Journal of
Mechanics of
Materials and Structures

INTERFACIAL MICROSCOPIC BOUNDARY CONDITIONS ASSOCIATED WITH BACKSTRESS-BASED HIGHER-ORDER GRADIENT CRYSTAL PLASTICITY THEORY

Mitsutoshi Kuroda

Volume 12, No. 2 March 2017

msp

JOURNAL OF MECHANICS OF MATERIALS AND STRUCTURES
Vol. 12, No. 2, 2017
dx.doi.org/10.2140/jomms.2017.12.193

INTERFACIAL MICROSCOPIC BOUNDARY CONDITIONS ASSOCIATED WITH BACKSTRESS-BASED HIGHER-ORDER GRADIENT CRYSTAL PLASTICITY THEORY

MITSUTOSHI KURODA

A strategy for modeling various interfacial boundary conditions associated with a higher-order gradient crystal plasticity theory is proposed. The gradient theory employed is based on the concept of the backstress that is produced in response to the spatial variation of the geometrically necessary dislocation densities. To set arbitrary interfacial boundary conditions for the crystallographic slip at the continuum level, a model with a single scalar quantity that aims to control the slipping rate at an interface is introduced. This scalar quantity is intended to represent the resultant effects of microscopic mechanisms such as absorption, emission, and transmission of the dislocations at an interface or a grain boundary (GB). As a realistic application of this basic idea, an orientation-dependent GB model is proposed, which incorporates effects of the degree of misorientation between the adjacent grains as well as the orientation of the GB plane relative to the grains. To illustrate capabilities of the proposed model, the bicrystalline micropillar compression problem is considered. Finite element simulations are performed for the bicrystalline micropillars including either a large-angle grain boundary (LAGB) or a coherent twin boundary (CTB) parallel to the compression axis. The numerical results are qualitatively compared with experimental observations reported in the literature. It is shown that the proposed GB model has a capability to represent the overall material responses associated with both LAGB and CTB using the same material parameter values.

1. Introduction

Size-dependent mechanical behaviors are usually observed in metallic materials at the micrometer or smaller scales. Predictions of size-dependent material responses are particularly important in the fields of small-scale electromechanical systems and nanostructured metallic materials. A considerable number of studies have been done so far with the aim of incorporating the size-effect into plasticity theories since the pioneering work of Aifantis [1984; 1987]. Since the studies of Kröner [1963] and Mindlin [1964], nonlocal or higher-order gradient effects in elasticity have been discussed and investigated (e.g., [Gutkin and Aifantis 1999; Bacca et al. 2013]).

The crystal plasticity theory (e.g., [Peirce et al. 1983; Asaro and Needleman 1985]) is a physically based model that accounts for the mechanisms of crystallographic slips in metals. However, it does not account for any size effects intrinsic in the materials. Extensions of the conventional crystal plasticity theory to incorporate the size effects have been proposed in many studies so far.

One of the methods of introducing the size effects into crystal plasticity theory is to formulate plastic-strain-gradient-dependent work hardening laws (e.g., [Acharya and Bassani 2000; Ohashi 2005]). Spatial

Keywords: strain gradient plasticity, crystal plasticity, interfaces, grain boundaries, geometrically necessary dislocations.

gradients of plastic strain (or crystallographic slips) correspond to the densities of geometrically necessary dislocations (GNDs) [Ashby 1970; Fleck et al. 1994]. The size effects can be introduced into conventional crystal plasticity models by assuming that the GNDs contribute to the increase in work hardening. In this type of modeling, only scalar quantities that represent the hardness of slip systems are augmented by a contribution from the GNDs. Therefore, the formulation of the boundary-value problem remains the same as that in the conventional theories. Only the tractions or prescribed displacements on the surfaces of a body are considered as the boundary conditions, and prescribing values of slips or their gradients at the boundaries is outside the scope.

Another method of incorporating the size effects, which is of interest in the present study, is higher-order extensions of the conventional theory (e.g., [Gurtin 2002; 2008a; Borg 2007; Yefimov et al. 2004b; Evers et al. 2004; Arsenlis et al. 2004; Bayley et al. 2006; Levkovitch and Svendsen 2006]). These higher-order theories open up the possibility of modeling extra boundary conditions for slips and their gradients at an interface or a grain boundary. Higher-order gradient crystal plasticity theories have been developed with two different trends so far. According to the classification proposed by Kuroda and Tvergaard [2008b], they are referred to as the "work-conjugate type" and "non-work-conjugate type" of theories. The first type is based on the concept of higher-order stresses that are introduced as work conjugates to spatial gradients of crystallographic slips and higher-order tractions that are postulated to exist as work conjugates to crystallographic slips on external surfaces or internal interfaces (e.g., [Gurtin 2002; 2008a]). This type introduces, as the major premise, a virtual work principle extended with the higher-order quantities and their work conjugates. Equilibrium or balance equations in the form of partial differential equations are derived from this premised virtual work statement. The second type is based on the concept of a *backstress*, that is, a long-range internal stress produced by an array of GNDs. The backstress effect can be incorporated directly into the conventional framework of a crystal plasticity theory (e.g., [Groma et al. 2003; Yefimov et al. 2004b; Evers et al. 2004; Arsenlis et al. 2004; Kuroda and Tvergaard 2006]). According to the classical dislocation theory, the spatial gradient of GND density is the origin of the backstress (equivalently, the internal stress), and superposition of the backstress and the externally induced resolved shear stress is taken to be an effective shear stress that activates slip deformations [Evers et al. 2004]. This second type of theory has a higher-order nature in the sense that extra boundary conditions for the crystallographic slips can be imposed, but it does not directly rely on higher-order stress quantities. Some mathematical equivalence between these two types of higher-order gradient crystal plasticity theories has been emphasized by Kuroda and Tvergaard [2008a; 2008b].

In the context of higher-order gradient crystal plasticity theories, two kinds of extreme extra boundary conditions have been mostly considered in previous applications. One is the *microscopically hard* condition, which supposes situations that all dislocations stop at the boundary and consequently the slip or its rate is fully constrained at the boundary. The other is the *microscopically free* condition, which assumes that the higher-order traction is zero in the work-conjugate type formulation [Gurtin 2002] or no GND density is required at the boundary in the non-work-conjugate type formulation [Evers et al. 2004; Kuroda and Tvergaard 2008b]. Gurtin and Needleman [2005] proposed a model of grain boundary behavior within the work-conjugate type framework, which accounts for a flow of the Burgers vector across the GB, and suggested, as an example, the *defect-free* condition, which assumes that the Burgers vector flow out of one grain is equal to that into the adjacent grain. Recently, Gurtin [2008b] has proposed another model of grain boundary conditions, which accounts for grain misorientation and grain-boundary

orientation relative to the grains. Van Beers et al. [2013] proposed a model of grain boundary interface mechanics based on a mixed treatment of the work-conjugate and non-work-conjugate formulations, in which the slip rates at the grain boundary are assumed to be governed by bulk-induced and energetic interfacial higher-order microforces. Ekh et al. [2011] proposed a grain boundary model in which a newly defined grain boundary microstress is assumed to activate the slip at the boundary, depending on the misorientation between the adjacent grains. Wulfinghoff et al. [2013] and Bayerschen et al. [2015] proposed a gradient plasticity model with an interface yield condition that accounts for the resistance of grain boundaries against plastic flow occurrence. They used an equivalent strain rather than slips on the individual slip systems as a fundamental field variable in order to simplify the formulation of the model.

Recently, for the purpose of clarifying the nature and roles of grain boundaries, experimental studies on bicrystalline micropillars have been conducted. Ng and Ngan [2009] and Imrich et al. [2014] independently showed that a large-angle grain boundary (LAGB) can act as a strong barrier to mobile dislocations, leading to a significant dislocation pile-up and an increase in dislocation density, for the size range (diameter or edge length of micropillars) of 6–7 μm. In contrast, Kunz et al. [2011] reported a completely opposite observation on submicron-sized bicrystalline pillars. The grain boundaries in their specimens seemed to act as sinks absorbing dislocations. Kim et al. [2015] stated that the LAGB in their submicrometer-sized bicrystalline pillar showed an ability to nucleate dislocations and did not act as a strong barrier to dislocations. These observations confirm that the nature of grain boundaries is complex and is not simply a function of the orientation of the boundary with respect to the grains or the relative misorientation of the grains. According to the studies of Ng and Ngan [2009], Kunz et al. [2011], and Imrich et al. [2014], for micropillars of different sizes, the distance from the grain boundary to the free surface may have some influence on the nature of the grain boundaries. Imrich et al. [2014] further carried out compression tests on a bicrystalline micropillar with a size of $\sim 4\,\mu$m and a coherent twin boundary (CTB). The CTB sample showed mechanical behavior very similar to that of single-crystalline samples, as if no grain boundary had existed. Hirouchi and Shibutani [2014] also conducted compression tests on copper bicrystalline micropillars with $\Sigma 3$ CTB and found that the bicrystalline micropillars exhibited a stress-strain response and deformation behavior fundamentally similar to those of single-crystalline micropillars having one of the crystal orientations that constitutes the bicrystalline micropillars.

In the present study, an alternative strategy for treating the higher-order interfacial boundary conditions within the non-work-conjugate type (or backstress-based) framework of the gradient crystal plasticity theory is proposed. To treat various interfacial boundary conditions for the crystallographic slip in a simplified manner, a model with a single scalar quantity that aims to control the slipping rate at an interface is introduced. This scalar quantity represents the resistance of an interface or a grain boundary to slip occurrence, which results from finer-scale phenomena such as absorption, emission, and transmission of the dislocations that are not resolved in the continuum modeling of crystal plasticity. As mentioned above, the grain boundary nature observed in experiments reported in the literature is complex. The real mechanism by which the observed grain boundary behavior is manifested has not been clarified sufficiently at present. Given this circumstance, the proposed model may seem to be rather phenomenological. However, it has plenty of room for extension, which can incorporate geometric relations of adjacent grains, grain boundary yielding, and many other phenomena that are likely to occur at the grain boundaries and internal interfaces. The present model may also be used to represent specific characteristics of external surfaces partially penetrable to dislocations, which may correspond to surfaces

having fragile oxide layers or microscopically incomplete contact surfaces. The first part of the paper is devoted to illustrating the basic idea of the proposed model and demonstration of its fundamental nature through analysis of a typical benchmark problem, i.e., the constrained simple shear problem. In the following parts, a generalization of the model and its application to a practical problem are presented. The bicrystalline micropillar compression problem is adopted to illustrate the efficiency of the proposed model.

2. Illustrations of basic idea

2.1. ***Backstress-based higher-order gradient crystal plasticity theory: the simplest version.*** To illustrate the fundamental nature of the proposition introduced in the present paper, we confine our attention to a backstress-based higher-order gradient crystal plasticity theory that is as simple as possible but not too simple [Kuroda and Tvergaard 2006]. In the subsequent sections that are devoted to its generalization and application to a practical problem, we will employ a much more generalized version of the theory [Kuroda and Tvergaard 2008a; 2008b].

Under a small strain assumption, the total strain rate $\dot{\boldsymbol{E}}$ is assumed to be decomposed into elastic and plastic parts:

$$\dot{\boldsymbol{E}} = (\nabla \otimes \dot{\boldsymbol{u}})_{\mathrm{sym}} = \dot{\boldsymbol{E}}^{\mathrm{e}} + \dot{\boldsymbol{E}}^{\mathrm{p}}, \tag{1}$$

where $\dot{\boldsymbol{u}}$ is the displacement rate vector, ∇ is the spatial gradient operator, $\otimes$ is the tensor product, the subscript sym denotes the symmetric part of the tensor, the superscripts e and p stand for "elastic" and "plastic", respectively, and a superposed dot denotes the material-time derivative.

Hooke's law is applied to represent elasticity,

$$\dot{\boldsymbol{E}}^{\mathrm{e}} = \boldsymbol{C}^{-1} : \dot{\boldsymbol{\sigma}}, \tag{2}$$

where $\boldsymbol{C}$ is a fourth-order elasticity modulus tensor, the superscript -1 denotes the tensor inverse, and $\boldsymbol{\sigma}$ is a symmetric (Cauchy) stress. Plastic deformation is assumed to take place through a single slip:

$$\dot{\boldsymbol{E}}^{\mathrm{p}} = \dot{\gamma}\, \boldsymbol{P}, \quad \boldsymbol{P} = (\boldsymbol{s} \otimes \boldsymbol{m})_{\mathrm{sym}}, \tag{3}$$

where $\dot{\gamma}$ is the slip rate, $\boldsymbol{s}$ and $\boldsymbol{m}$ are the unit vectors specifying the slip direction and slip plane normal, respectively, and $\boldsymbol{P}$ is the Schmid tensor. In this simplified theory, it is assumed that $\boldsymbol{s}$ and $\boldsymbol{m}$ constitute a planar slip system, i.e., they are both on the X_1-X_2 plane and $\boldsymbol{p} = \boldsymbol{s} \times \boldsymbol{m}$ is parallel to the X_3-axis.

The yield plane in the stress space is defined by

$$f = |\tau - \tau_{\mathrm{b}}| - g = 0, \tag{4}$$

where τ, τ_{b}, and g are the resolved shear stress (RSS), backstress, and critical resolved shear stress (CRSS) respectively given by

$$\tau = \boldsymbol{\sigma} : \boldsymbol{P}, \quad \tau_{\mathrm{b}} = \beta \nabla \rho_{\mathrm{G}} \cdot \boldsymbol{s}, \quad g = \tau_0 + h \int_0^t |\dot{\gamma}|\, \mathrm{d}t. \tag{5}$$

Here, ρ_{G} is the geometrically necessary dislocation (GND) density, β is a coefficient for dimensional consistency with dimensions of [force $\times$ length], which is assumed to be constant, τ_0 is an initial value

of CRSS, h is a slip hardening modulus taken to be constant for simplicity, and t is time. The GND density ρ_{G} must satisfy the relation [Ashby 1970; Arsenlis and Parks 1999]

$$\rho_{\mathrm{G}} + \frac{1}{b}\nabla\gamma \cdot \boldsymbol{s} = 0, \tag{6}$$

where b is the magnitude of the Burgers vector. Note that ρ_{G} in $(5)_2$ and (6) represents the density of edge-type GNDs[1] as we consider the planar slip system.

For continued plastic deformation, the stress point must remain on the yield plane; therefore,

$$\dot{f} = \frac{\partial \tau}{\partial \boldsymbol{\sigma}} : \dot{\boldsymbol{\sigma}} - \beta \nabla \dot{\rho}_{\mathrm{G}} \cdot \boldsymbol{s} - h\dot{\gamma} = 0, \tag{7}$$

which leads to

$$\dot{\gamma} = \frac{\boldsymbol{P} : \boldsymbol{C} : \dot{\boldsymbol{E}} - \beta \nabla \dot{\rho}_{\mathrm{G}} \cdot \boldsymbol{s}}{A}, \quad A = \boldsymbol{P} : \boldsymbol{C} : \boldsymbol{P} + h. \tag{8}$$

In the derivation of the above relation, it is assumed that the signs of $\dot{\gamma}$ and $\tau - \tau_{\mathrm{b}}$ are identified. Substituting (8) into (3), and combining it with (2) and (1), we have the elastoplasticity constitutive relation

$$\dot{\boldsymbol{\sigma}} = \boldsymbol{C}^{\mathrm{ep}} : \dot{\boldsymbol{E}} + \frac{\beta}{A}\boldsymbol{C} : \boldsymbol{P} \nabla \dot{\rho}_{\mathrm{G}} \cdot \boldsymbol{s}, \tag{9}$$

where

$$\boldsymbol{C}^{\mathrm{ep}} = \boldsymbol{C} - \frac{1}{A}(\boldsymbol{C} : \boldsymbol{P}) \otimes (\boldsymbol{P} : \boldsymbol{C}). \tag{10}$$

Now, we introduce an incremental form of the virtual work principle as

$$\int_V \dot{\tilde{\boldsymbol{E}}} : \dot{\boldsymbol{\sigma}} \, \mathrm{d}V = \int_{S_t} \dot{\tilde{\boldsymbol{u}}} \cdot \dot{\underline{\boldsymbol{t}}} \, \mathrm{d}S, \quad \dot{\tilde{\boldsymbol{E}}} = (\dot{\tilde{\boldsymbol{u}}} \otimes \nabla)_{\mathrm{sym}}. \tag{11}$$

Here, $\dot{\tilde{\boldsymbol{u}}}$ is the virtual displacement rate that takes zero on part of the surface, S_u, where real displacement rates are prescribed, otherwise it can take any arbitrary value, and $\dot{\underline{\boldsymbol{t}}}$ is the surface traction rate prescribed on the remaining part of the surface, S_t (recall that formally we write $S = S_t \cup S_u$ with the total surface S of the body under consideration). Substituting (9) into (11) gives

$$\int_V \dot{\tilde{\boldsymbol{E}}} : \boldsymbol{C}^{\mathrm{ep}} : \dot{\boldsymbol{E}} \, \mathrm{d}V + \int_V \dot{\tilde{\boldsymbol{E}}} : \boldsymbol{C} : \boldsymbol{P} \frac{\beta}{A} \nabla \dot{\rho}_{\mathrm{G}} \cdot \boldsymbol{s} \, \mathrm{d}V = \int_{S_t} \dot{\tilde{\boldsymbol{u}}} \cdot \dot{\underline{\boldsymbol{t}}} \, \mathrm{d}S. \tag{12}$$

Equation (12) has two independent variables, $\dot{\boldsymbol{u}}$ and $\dot{\rho}_{\mathrm{G}}$, which cannot be determined by a single equation.

Now, we view (6) as an additional governing equation implying that the GND density balances with the spatial gradient of a slip in the slip direction. A weak form of the incremental relation of (6) becomes

$$\int_V \tilde{\rho}\dot{\rho}_{\mathrm{G}} \, \mathrm{d}V - \int_V \frac{1}{b}\nabla\tilde{\rho} \cdot \boldsymbol{s}\dot{\gamma} \, \mathrm{d}V = -\int_{S_\gamma} \frac{1}{b}\tilde{\rho}\boldsymbol{n} \cdot \boldsymbol{s}\underline{\dot{\gamma}} \, \mathrm{d}S, \tag{13}$$

where $\tilde{\rho}$ is a virtual weighting function that is zero on part of the surface, S_ρ, where $\dot{\rho}_{\mathrm{G}}$ is prescribed, otherwise it can take any arbitrary value, $\boldsymbol{n}$ is a unit normal to the boundary, and $\underline{\dot{\gamma}}$ is a slip rate prescribed

[1] Different researchers sometimes use different sign conventions for the GND densities. The sign convention for the edge-type GND density in (6) follows that introduced by Arsenlis and Parks [1999].

on part of the surface, S_γ (formally we consider $S = S_\rho \cup S_\gamma$), except for the special case of $\boldsymbol{n}\cdot\boldsymbol{s} = 0$, where $\underline{\dot{\gamma}}$ must be free of any constraint. Substituting (8) into (13) gives

$$-\int_V \frac{1}{bA}\nabla\tilde{\rho}\cdot(\boldsymbol{s}\otimes\boldsymbol{P}):\boldsymbol{C}:\dot{\boldsymbol{E}}\,\mathrm{d}V + \int_V\left[\tilde{\rho}\dot{\rho}_{\mathrm{G}} + \frac{\beta}{bA}\nabla\tilde{\rho}\cdot(\boldsymbol{s}\otimes\boldsymbol{s})\cdot\nabla\dot{\rho}_{\mathrm{G}}\right]\mathrm{d}V = -\int_{S_\gamma}\frac{1}{b}\tilde{\rho}\boldsymbol{n}\cdot\boldsymbol{s}\underline{\dot{\gamma}}\,\mathrm{d}S. \quad (14)$$

2.2. ***Treatment of microscopic boundary conditions: a proposition.*** In previous studies [Evers et al. 2004; Kuroda and Tvergaard 2006; 2008a; 2008b], the following two types of microscopic boundary condition have been considered:

- Microscopically hard condition:

$$\boldsymbol{n}\cdot\boldsymbol{s}\underline{\dot{\gamma}} = 0, \quad (15)$$

- Microscopically free condition:

$$\dot{\rho}_{\mathrm{G}} = 0. \quad (16)$$

In general cases of $\boldsymbol{n}\cdot\boldsymbol{s} \neq 0$, (15) is equivalent to $\underline{\dot{\gamma}} = 0$.

An alternative representation of the microscopic boundary conditions is considered. Suppose that the value of $\underline{\dot{\gamma}}$ coincides with $\dot{\gamma}$ given by (8) for $\boldsymbol{n}\cdot\boldsymbol{s} \neq 0$. In this case, the boundary is said to be *transparent*, i.e., it possesses the same property as that of the bulk part of the material. Now, we formally write the slip rate at the boundary as

$$\underline{\dot{\gamma}} = \phi\dot{\gamma}, \quad (17)$$

where ϕ is a dimensionless scalar quantity. Then, the two extreme boundary conditions can be written as

$$\phi = 1 \text{ for the transparent condition,} \quad (18)$$

$$\phi = 0 \text{ for the microscopically hard condition.} \quad (19)$$

Thus, the domain of ϕ is naturally assumed to be

$$0 \le \phi \le 1. \quad (20)$$

A value of ϕ within $0 < \phi < 1$ gives a relaxed microscopic boundary condition for the slip at an interface.

Substituting (17) with (8) into (14) gives

$$-\int_V \frac{1}{bA}\nabla\tilde{\rho}\cdot(\boldsymbol{s}\otimes\boldsymbol{P}):\boldsymbol{C}:\dot{\boldsymbol{E}}\,\mathrm{d}V + \int_{S_\gamma}\frac{\phi}{bA}\tilde{\rho}\boldsymbol{n}\cdot(\boldsymbol{s}\otimes\boldsymbol{P}):\boldsymbol{C}:\dot{\boldsymbol{E}}\,\mathrm{d}S$$
$$+\int_V\left[\tilde{\rho}\dot{\rho}_{\mathrm{G}} + \frac{\beta}{bA}\nabla\tilde{\rho}\cdot(\boldsymbol{s}\otimes\boldsymbol{s})\cdot\nabla\dot{\rho}_{\mathrm{G}}\right]\mathrm{d}V - \int_{S_\gamma}\frac{\phi\beta}{bA}\tilde{\rho}\boldsymbol{n}\cdot(\boldsymbol{s}\otimes\boldsymbol{s})\cdot\nabla\dot{\rho}_{\mathrm{G}}\,\mathrm{d}S = 0. \quad (21)$$

The present treatment of the boundary may also represent specific characteristics of external surfaces. For example, a strongly passivated surface is modeled by $\phi = 0$, and an external surface coated by an incomplete or fragile thin oxide layer that is partially penetrable to dislocations may be modeled by $0 < \phi < 1$. It is noted that Yefimov et al. [2004a] have assumed a condition equivalent to $\phi = 1$ (i.e., $\underline{\dot{\gamma}} = \dot{\gamma}$) to represent a perfect free surface of a bent foil specimen.

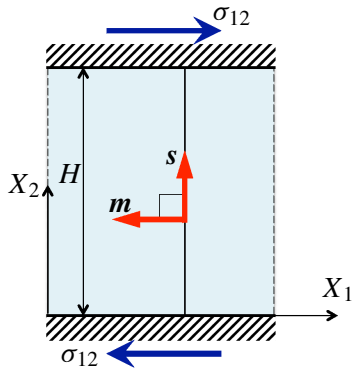

Figure 1. Constrained simple shear problem of a strip with an infinite lateral length and a single slip system whose slip direction is parallel to the thickness direction. The microscopically hard condition is imposed on the bottom surface, whereas flexible boundary conditions ($0 \le \phi \le 1$) are adopted on the upper surface.

2.3. ***Finite element equation.*** A finite element equation for the present model is derived straightforwardly from (12) and (21), choosing $\dot{\boldsymbol{u}}$ and $\dot{\rho}_{\mathrm{G}}$ as the nodal quantities to be solved. It is written as

$$\begin{bmatrix} \boldsymbol{K}_{(uu)} & \boldsymbol{K}_{(u\rho)} \\ \boldsymbol{K}_{(\rho u)} & \boldsymbol{K}_{(\rho\rho)} \end{bmatrix} \begin{Bmatrix} \dot{\boldsymbol{U}} \\ \dot{\boldsymbol{P}}_{\mathrm{G}} \end{Bmatrix} = \begin{Bmatrix} \dot{\boldsymbol{F}} \\ \boldsymbol{0} \end{Bmatrix}, \tag{22}$$

where $\{\dot{\boldsymbol{U}}\}$ is a vectorial array of nodal values of $\dot{\boldsymbol{u}}$, $\{\dot{\boldsymbol{P}}_{\mathrm{G}}\}$ is a vectorial array of nodal values of $\dot{\rho}_{\mathrm{G}}$, $[\boldsymbol{K}_{(\mathrm{ab})}]$ (where "a" and "b" stand for "u" or "ρ") are the corresponding stiffness matrices, and $\{\dot{\boldsymbol{F}}\}$ is a vectorial array of nodal forces, which corresponds to the right-hand side of (12). Actual numerical computations are performed using an adoptive forward Euler time integration scheme proposed by Yamada et al. [1968].

2.4. ***Illustrative examples.*** To illustrate the effects of the proposed microscopic boundary conditions, the constrained simple shear problem is considered. A strip with a height H in the X_2-direction and an infinite length in the X_1-direction is subjected to simple shear (Figure 1). This material has only one slip system whose slip direction and slip plane normal coincide with X_2- and negative X_1-directions, respectively. The bottom surface is assumed to act as a microscopically hard boundary (i.e., $\phi = 0$), whereas various values of ϕ in the range $0 \le \phi \le 1$ are applied to the top surface to see the fundamental nature of the proposed boundary model. The displacement rate $\dot{U}$ in the X_1-direction on the top surface is prescribed, and the macroscopic shear strain Γ is defined as $\Gamma = U/H$.

The thickness of the strip is discretized with 60 quadrilateral elements in the thickness (X_2-) direction, and only one element is assigned in the lateral (X_1-) direction. Periodic conditions are applied to both sides of the finite element model. The serendipity shape functions are used to interpolate the displacement rate field, while the bilinear shape functions are employed to interpolate the GND density rate field. The coordinates of the nodes in the bilinear four-node elements are set to be identical to those of the corner nodes in the serendipity eight-node elements. The Gaussian quadrature with 2×2 points is used for volume integrals and that with 2 points is used for surface integrals. This combination of the

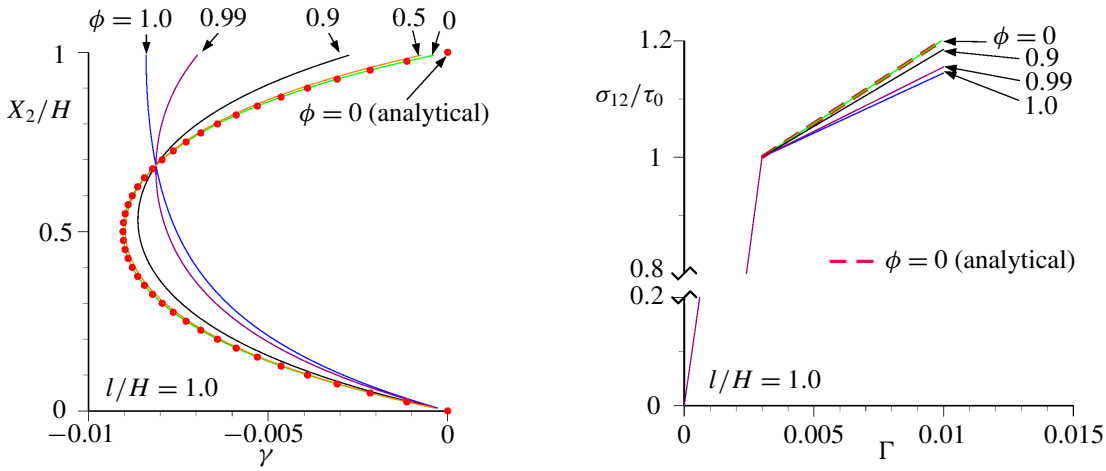

Figure 2. Computational results for constrained simple shear problem with relaxed microscopic boundary conditions at the upper surface for a relative length scale of $l/H = 1.0$. Distributions of slip in the thickness direction at a macroscopic shear strain Γ of 0.01 (left). Curves of shear stress versus macroscopic shear strain (right).

shape functions and the Gaussian quadrature order gives satisfactory numerical results free of volumetric locking and unexpected stress oscillation phenomena [Kuroda 2011; 2015].

The material constants are $\mu/\tau_0 = 333.3$ (μ is the shear elastic modulus) and $h/\tau_0 = 16.67$. The coefficient β in $(5)_2$ is formulated as

$$\beta = l^2 b \tau_0, \tag{23}$$

where l is a constant material length scale.

The responses of the strip with a size of $l/H = 1$ are shown in Figure 2. The distributions of slip γ in the X_2-direction at $\Gamma = 0.01$ are depicted[2] in Figure 2 (left) for ϕ values of $0 \le \phi \le 1$. Curves of the shear stress σ_{12} (that equals $-\tau$) versus Γ are plotted in Figure 2 (right). For $\phi = 0$ (i.e., the microscopically hard condition), the analytical solution [Bittencourt et al. 2003] is also shown to validate the quality of the present finite element solutions. In Figure 2 (left), it is seen that the constraint on γ at $X_2 = H$ is released with the increase in ϕ. The slip distribution profile for $\phi = 0.5$ is comparable to that for $\phi = 0$. Even for $\phi = 0.9$, the value of γ at $X_2 = H$ is still smaller than half of the maximum of γ. In the range of $\phi > 0.9$, the slip distribution profile is sensitively changed with ϕ. For $\phi = 1$, the condition of $\mathrm{d}\dot{\gamma}/\mathrm{d}X_2 = 0$ (equivalently, $\dot{\rho}_{\mathrm{G}} = 0$ in this case) is established.

The distributions of slip at $\Gamma = 0.01$ for a relative length scale of $l/H = 0.3$ are depicted in Figure 3. In this case, clear *boundary layers* are formed. The overall behavior associated with the change in ϕ is similar to that for $l/H = 1$. Variation of the stress-strain curves due to a change in the interfacial

[2]The values of γ are computed at the Gaussian points and they are constant within each element in the present problem. The smoothly plotted curves shown in Figure 2 (left), as well as in Figure 3, are obtained using the values of γ evaluated at the positions of the *corner nodes* as the average of values in the adjacent elements. However, the values at the boundaries of the body cannot be evaluated in this manner. Thus, the computed curves do not reach the boundaries at $X_2/H = 0$ and 1 in Figures 2 (left) and 3.

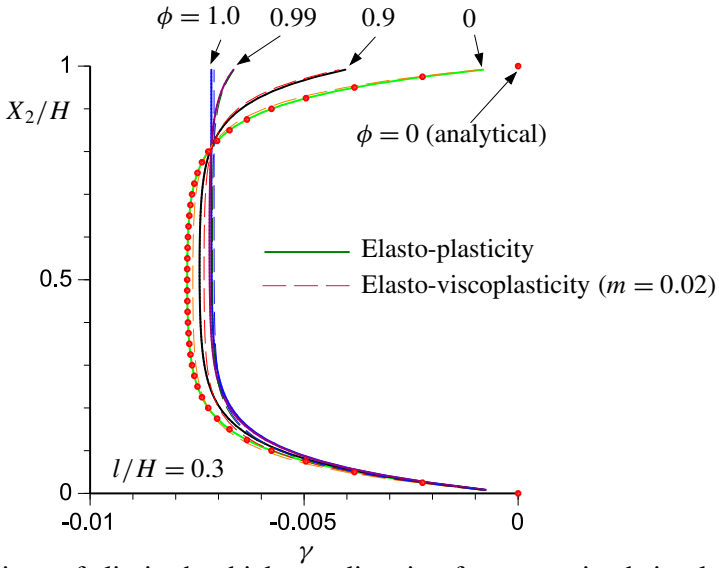

Figure 3. Distributions of slip in the thickness direction for constrained simple shear problem with relaxed microscopic boundary conditions at the upper surface for a relative length scale of $l/H = 0.3$ at $\Gamma = 0.01$.

microscopic boundary conditions is very small in the case of $l/H = 0.3$, and their depiction is omitted. The trend is fundamentally the same as that shown in Figure 2 (right) for $l/H = 1.0$.

In addition to the rate-independent elasto-plasticity analysis, an elasto-viscoplastic version of the theory, which has been frequently employed in previous studies [Kuroda and Tvergaard 2006; 2008a; 2008b; El-Naaman et al. 2016], is examined here. The power law relation is used, instead of the yield condition (4), given as

$$\dot{\gamma} = \operatorname{sgn}(\tau - \tau_{\mathrm{b}})\dot{\gamma}_0 \left(\frac{|\tau - \tau_{\mathrm{b}}|}{g} \right)^{1/m}, \tag{24}$$

where m is a rate sensitivity exponent and $\dot{\gamma}_0$ is a reference slip rate. In the present example, m is chosen to be 0.02, which is a realistic value for common metals at room temperature, and $\dot{\gamma}_0$ is identified with $\dot{\Gamma}$ in the computations. In the limit $m \to 0$, (24) reduces to (4). In the finite element computations of the elasto-viscoplastic version, (13) is directly used for the GND density analysis, as in previous studies [Kuroda and Tvergaard 2006; 2008a; 2008b]. Equation (17) with (24) is applied to the right-hand side of (13). It has been confirmed that the responses of an elasto-viscoplastic material governed by (24) with the microscopic boundary conditions prescribed by the use of (17) approximate the corresponding elasto-plasticity responses, as observed in Figure 3. Note that an extrapolation is required to evaluate a value of $\dot{\gamma}$ at the edge of the element at the boundary because $\dot{\gamma}$ is computed inside the element in the present theory. In the present simple shear problem with the finite element type used here, the value of $\dot{\gamma}$ is constant within each element, and this constant value has been used as the extrapolated value at the edge of the element at the upper end of the finite element model. The effect of such extrapolation on the solution is subordinated in an appropriately discretized finite element meshing.

2.5. ***Three-dimensional, multislip description of the theory.*** In the above, we confined our attention to the simplified theory with a single-slip system in the two-dimensional setting to illustrate the basic idea of

the interfacial boundary condition newly proposed. The three-dimensional form of the theory with multi-slip systems (but still in the small strain regime [Kuroda and Tvergaard 2008b]) is briefly described below.

For multislip conditions, adoption of the viscoplastic formulation is advantageous because it is free from the problem of the unique determination of the slip rate on each slip system, which is encountered in rate-independent crystal plasticity analyses. Thus, (24) is extended to

$$\dot{\gamma}^{(\alpha)} = \operatorname{sgn}(\tau^{(\alpha)} - \tau_{\mathrm{b}}^{(\alpha)})\dot{\gamma}_0 \left(\frac{|\tau^{(\alpha)} - \tau_{\mathrm{b}}^{(\alpha)}|}{g^{(\alpha)}} \right)^{1/m}, \tag{25}$$

where α is the slip system number, and

$$\tau^{(\alpha)} = \boldsymbol{\sigma} : \boldsymbol{P}^{(\alpha)}; \quad \boldsymbol{P}^{(\alpha)} = (\boldsymbol{s}^{(\alpha)} \otimes \boldsymbol{m}^{(\alpha)})_{\mathrm{sym}}, \tag{26}$$

$$g^{(\alpha)} = \tau_0 + \int_0^t \sum_{\beta} h^{(\alpha\beta)} |\dot{\gamma}^{(\beta)}| \, \mathrm{d}t, \tag{27}$$

$$\tau_{\mathrm{b}}^{(\alpha)} = l^2 b \tau_0 (\nabla \rho_{\mathrm{G(e)}}^{(\alpha)} \cdot \boldsymbol{s}^{(\alpha)} + \nabla \rho_{\mathrm{G(s)}}^{(\alpha)} \cdot \boldsymbol{p}^{(\alpha)}). \tag{28}$$

Here, $h^{(\alpha\beta)}$ is a slip hardening moduli matrix that can incorporates latent hardening effects[3], $\rho_{\mathrm{G(e)}}^{(\alpha)}$ is the density of the edge-type GNDs, $\rho_{\mathrm{G(s)}}^{(\alpha)}$ is the density of the screw-type GNDs, and $\boldsymbol{p}^{(\alpha)} = \boldsymbol{s}^{(\alpha)} \times \boldsymbol{m}^{(\alpha)}$. In (28), interactions between the slip systems are neglected for simplicity within the present paper. More elaborate backstress models with the slip system interactions were proposed by Evers et al. [2004] and Bayley et al. [2006], and were used in [Kuroda and Tvergaard 2008a; 2008b] and [Kuroda 2013].

Weak forms of the incremental relations of the edge- and screw-type GND density balances[4] are, respectively,

$$\int_V \tilde{\rho} \dot{\rho}_{\mathrm{G(e)}}^{(\alpha)} \, \mathrm{d}V - \int_V \frac{1}{b} \nabla \tilde{\rho} \cdot \boldsymbol{s}^{(\alpha)} \dot{\gamma}^{(\alpha)} \, \mathrm{d}V = - \int_{S_\gamma} \frac{1}{b} \tilde{\rho} \boldsymbol{n} \cdot \boldsymbol{s}^{(\alpha)} \underline{\dot{\gamma}}^{(\alpha)} \, \mathrm{d}S, \tag{29}$$

$$\int_V \tilde{\rho} \dot{\rho}_{\mathrm{G(s)}}^{(\alpha)} \, \mathrm{d}V - \int_V \frac{1}{b} \nabla \tilde{\rho} \cdot \boldsymbol{p}^{(\alpha)} \dot{\gamma}^{(\alpha)} \, \mathrm{d}V = - \int_{S_\gamma} \frac{1}{b} \tilde{\rho} \boldsymbol{n} \cdot \boldsymbol{p}^{(\alpha)} \underline{\dot{\gamma}}^{(\alpha)} \, \mathrm{d}S, \tag{30}$$

with

$$\underline{\dot{\gamma}}^{(\alpha)} = \phi^{(\alpha)} \dot{\gamma}^{(\alpha)}. \tag{31}$$

A finite strain version of the theory has been given in [Kuroda and Tvergaard 2008a]. Equations for the finite strain version are not repeated here for brevity.

3. Strategy for generalization of $\phi^{(\alpha)}$

Consider a body composed of two parts (which may be grains), A and B, with a grain boundary (GB) or an interface S_{GB} (Figure 4). Under multislip situations, the expression of the present boundary model (17) is extended to

$$\underline{\dot{\gamma}}_{\mathrm{A}}^{(\alpha)} = \phi_{\mathrm{A}}^{(\alpha)} \dot{\gamma}_{\mathrm{A}}^{(\alpha)} \text{ on } S_{\mathrm{GB(A)}} \quad \text{and} \quad \underline{\dot{\gamma}}_{\mathrm{B}}^{(\beta)} = \phi_{\mathrm{B}}^{(\beta)} \dot{\gamma}_{\mathrm{B}}^{(\beta)} \text{ on } S_{\mathrm{GB(B)}}, \tag{32}$$

[3]Recently, a model of size-dependent latent hardening has been proposed by Bardella et al. [2013]. Such an effect has yet to be introduced in the present model.

[4]Different researchers use different sign conventions for the screw-type GND density. The sign convention for the screw-type GND density in (30) follows that used by Gurtin [2002; 2008b].

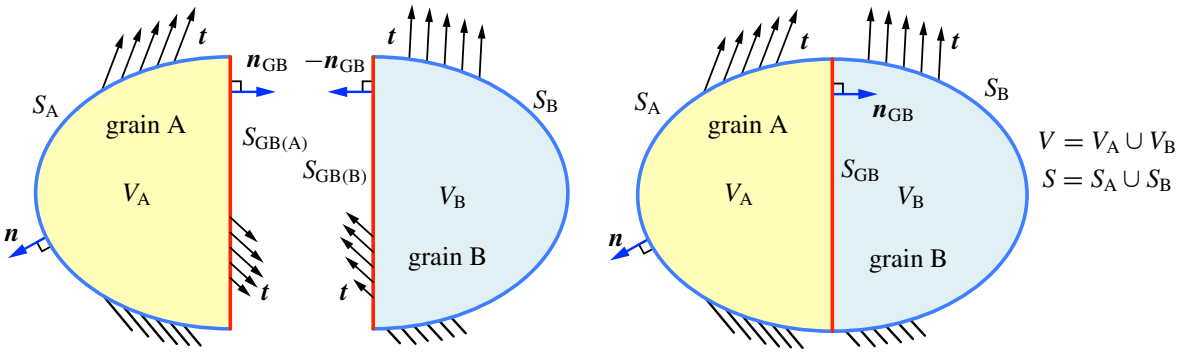

Figure 4. Schematic illustration of a body with a grain boundary. Separated description of grains A and B (left); grains A and B joined into a single body (right).

where the subscripts A and B denote that the corresponding quantities belongs to grain A or B, and the superscript α and β represent the slip system number given within grains A and B, respectively, and $S_{GB(A)}$ and $S_{GB(B)}$ are the interfacial surfaces seen from grains A and B, respectively. In general, the continuum modeling of crystal plasticity, in which crystallographic slips are taken as a fundamental deformation process, cannot directly resolve the individual dislocation behaviors such as absorption, emission (or subsequent reemission), and transmission, which would be observed at a finer scale. The resultant amount of slip rate resulting from these multiple phenomena is quantified via $\phi_I^{(i)}$ (with $I = \mathrm{A}$ or B and $i = \alpha$ or β for brevity). The coefficient $\phi_I^{(i)}$ is said to give a mesoscopic representation of the resistance of the interface to slip occurrence. In this modeling, the value of $\phi_{\mathrm{A}}^{(\alpha)}$ for grain A may be determined independently of information from grain B, and vice versa, for a supposed situation where the boundary on the grain A side acts as the dislocation sink and source, whereas the boundary on the grain B side functions as a strong barrier to dislocations. On the other hand, it is possible to consider grain interactions. Even in that case, it is reasonable to consider that $\phi_I^{(i)}$ does not become more than unity because the slip behavior at a point infinitesimally close to the GB must be governed by the mechanical conditions at that point located *inside* the grain. A negative $\phi_I^{(i)}$ is also inconsistent with the mechanical conditions at the point infinitesimally close to the GB. Available experimental data is not sufficient for formulating a unique form for the function $\phi_I^{(i)}$. However, it is generally expected that $\phi_I^{(i)}$ will be affected by a relative misorientation of the grains; the orientation of the GB relative to the grains; the spacing between the GB and the external surface; the thickness, structure, and amount of precipitation of the GB; temperature; and maybe some other factors.

In the current modeling, $\dot{\underline{\gamma}}_{\mathrm{A}}^{(\alpha)}$ at a point on the grain A side of the interface depends only on the slip rate $\dot{\gamma}_{\mathrm{A}}^{(\alpha)}$ in grain A. One might conceive a more elaborate and complicated formulation of $\dot{\underline{\gamma}}_{\mathrm{A}}^{(\alpha)}$ that also incorporates the influences of the slip rates $\dot{\gamma}_{\mathrm{B}}^{(\beta)}$ in grain B. This coupling, which induces a significant complexity in the formulation and computational procedure, is omitted in the present study. Nevertheless, this simple model has the capability to represent a rather wide range of material responses at the micrometer scale, as will be demonstrated in the next section.

In the following application, we consider a simple formulation that only takes into account the geometrical configuration of the slip systems and the GB plane (i.e., the degree of misorientation between

grains A and B, and the orientation of the GB plane relative to the grains):

$$\phi_{\mathrm{A}}^{(\alpha)} = (\max_{\beta} \bar{C}_{\mathrm{AB}}^{(\alpha\beta)})^{\nu}, \quad \phi_{\mathrm{B}}^{(\beta)} = (\max_{\alpha} \bar{C}_{\mathrm{AB}}^{(\alpha\beta)})^{\nu}, \tag{33}$$

where ν (≥ 0) is a scaling exponent, and the moduli $\bar{C}_{\mathrm{AB}}^{(\alpha\beta)}$ represent the degree of misorientation between the two adjacent grains and the GB orientation relative to those grains. The moduli $\bar{C}_{\mathrm{AB}}^{(\alpha\beta)}$ are given by

$$\begin{aligned} \bar{C}_{\mathrm{AB}}^{(\alpha\beta)} &= \left| \boldsymbol{s}_{\mathrm{A}}^{(\alpha)} \cdot \boldsymbol{s}_{\mathrm{B}}^{(\beta)} \right| \left| \bar{\boldsymbol{q}}_{\mathrm{A}}^{(\alpha)} \cdot \bar{\boldsymbol{q}}_{\mathrm{B}}^{(\beta)} \right|, \\ \bar{\boldsymbol{q}}_{\mathrm{A}}^{(\alpha)} &= \frac{\boldsymbol{m}_{\mathrm{A}}^{(\alpha)} \times \boldsymbol{n}_{\mathrm{GB}}}{\| \boldsymbol{m}_{\mathrm{A}}^{(\alpha)} \times \boldsymbol{n}_{\mathrm{GB}} \|}, \quad \bar{\boldsymbol{q}}_{\mathrm{B}}^{(\beta)} = \frac{\boldsymbol{m}_{\mathrm{B}}^{(\beta)} \times \boldsymbol{n}_{\mathrm{GB}}}{\| \boldsymbol{m}_{\mathrm{B}}^{(\beta)} \times \boldsymbol{n}_{\mathrm{GB}} \|}, \end{aligned} \tag{34}$$

where $\boldsymbol{n}_{\mathrm{GB}}$ is the GB normal that points from grain A to grain B, and $\boldsymbol{s}_I^{(i)}$ and $\boldsymbol{m}_I^{(i)}$ are respectively the slip direction and the slip plane normal that constitute the slip systems in each grain. The condition $0 \leq \bar{C}_{\mathrm{AB}}^{(\alpha\beta)} \leq 1$ leads to $0 \leq \phi_I^{(i)} \leq 1$. The basic idea for $\bar{C}_{\mathrm{AB}}^{(\alpha\beta)}$ can be found in [Clark et al. 1992], and it has recently been employed by Knorr et al. [2015] and Kheradmand et al. [2016] to evaluate the *slip transfer resistance of neighboring grains*[5] in problems of crack initiation at grain boundaries and deformation in micrometer-sized bicrystals. Figure 5 shows a schematic diagram of the geometrical configuration of the slip systems and the GB plane, which characterize values of $\bar{C}_{\mathrm{AB}}^{(\alpha\beta)}$. Using $\kappa_{\mathrm{AB}}^{(\alpha\beta)}$ to denote the angle between intersection lines of opposite slip planes from the neighboring grains on the GB plane and $\theta_{\mathrm{AB}}^{(\alpha\beta)}$ to denote the angle between the slip directions of opposite slip systems of the neighboring grains, then we can write $\bar{C}_{\mathrm{AB}}^{(\alpha\beta)} = |\cos\theta_{\mathrm{AB}}^{(\alpha\beta)}||\cos\kappa_{\mathrm{AB}}^{(\alpha\beta)}|$. In the current formulation of (33), the slip resistance is determined by the most orientationally favorable slip system in the neighboring grain, which has the largest value of $\bar{C}_{\mathrm{AB}}^{(\alpha\beta)}$. One of the most critical situations described using this model may be coherent twin boundaries (CTBs). Consider that the slip system α in grain A and the slip system β in grain B have the same Burgers vector that is parallel to the CTB plane (i.e., a cross slip occurs across the CTB). Thus, $\phi_I^{(i)}$ takes unity regardless of the value of ν since $\bar{C}_{\mathrm{AB}}^{(\alpha\beta)}$ takes unity. This represents a fully transparent characteristic of the GB showing no resistance to slip occurrence. It is noted that Gurtin [2008b] derived similar grain interaction moduli,

$$C_{\mathrm{AB}}^{(\alpha\beta)} = \boldsymbol{s}_{\mathrm{A}}^{(\alpha)} \cdot \boldsymbol{s}_{\mathrm{B}}^{(\beta)} (\boldsymbol{m}_{\mathrm{A}}^{(\alpha)} \times \boldsymbol{n}_{\mathrm{GB}}) \cdot (\boldsymbol{m}_{\mathrm{B}}^{(\beta)} \times \boldsymbol{n}_{\mathrm{GB}}) \quad \text{for} \quad 0 \leq |C_{\mathrm{AB}}^{(\alpha\beta)}| \leq 1,$$

in the context of a different modeling of the GB. The main difference between (34) and Gurtin's moduli is whether $\boldsymbol{m}_I^{(i)} \times \boldsymbol{n}_{\mathrm{GB}}$ are normalized to unit vectors. The values of $|C_{\mathrm{AB}}^{(\alpha\beta)}|$ do not reach unity for the pair of slip systems positioned in the cross slip configuration at the GB. If $|C_{\mathrm{AB}}^{(\alpha\beta)}|$ is used in (33), such a model shows a GB response harder than that predicted using $\bar{C}_{\mathrm{AB}}^{(\alpha\beta)}$.

When $\boldsymbol{m}_I^{(i)}$ is parallel to $\boldsymbol{n}_{\mathrm{GB}}$, then the value of $\bar{\boldsymbol{q}}_I^{(i)}$ is indeterminant, but simultaneously $\boldsymbol{s}_I^{(i)} \cdot \boldsymbol{n}_{\mathrm{GB}} = 0$. In this case, $\dot{\gamma}_I^{(i)}$ is free from constraint,[6] as is understood directly from (13). The interpretation that a GB parallel to the slip plane does not act as an obstacle to slip deformation is physically acceptable [Kuroda and Tvergaard 2008b].

[5] Kheradmand et al. [2016] defined the grain boundary transmission factor as $\omega_{\mathrm{AB}}^{(\alpha\beta)} = 1 - |\boldsymbol{s}_{\mathrm{A}}^{(\alpha)} \cdot \boldsymbol{s}_{\mathrm{B}}^{(\beta)}||\bar{\boldsymbol{q}}_{\mathrm{A}}^{(\alpha)} \cdot \bar{\boldsymbol{q}}_{\mathrm{B}}^{(\beta)}| = 1 - |\cos\theta_{\mathrm{AB}}^{(\alpha\beta)}||\cos\kappa_{\mathrm{AB}}^{(\alpha\beta)}|$. The angles $\theta_{\mathrm{AB}}^{(\alpha\beta)}$ and $\kappa_{\mathrm{AB}}^{(\alpha\beta)}$ are depicted in Figure 5. They used $\omega_{\mathrm{AB}}^{(\alpha\beta)}$ in the context of the qualitative interpretation of their experimental results, and they did not apply it to numerical simulations.

[6] In the actual numerical computations, use of an arbitrary value of $\bar{C}_{\mathrm{AB}}^{(\alpha\beta)}$ for the case of $\boldsymbol{s}_I^{(i)} \cdot \boldsymbol{n}_{\mathrm{GB}} = 0$ is sufficient to get the exact solution of the interfacial slip rate.

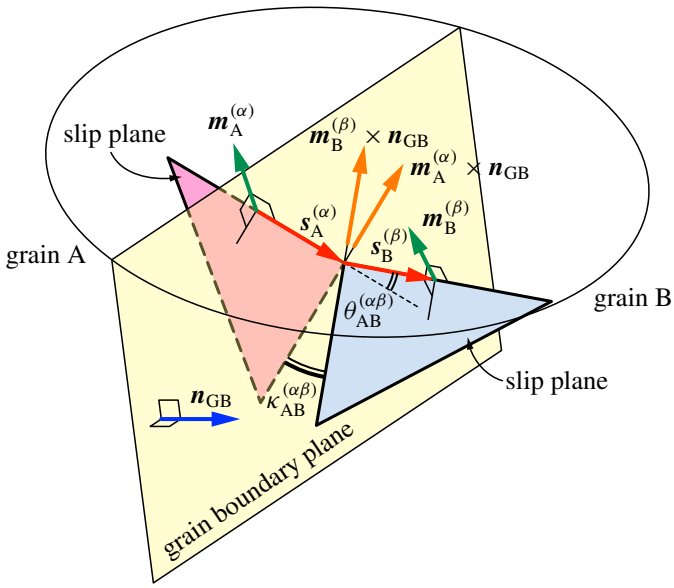

Figure 5. Schematic diagram of the geometrical configuration of the slip systems and the GB plane.

When $\nu = 1$, it is assumed that the amount of the interfacial slip depends linearly on the geometrical configuration of the GB plane and adjacent grains. A value of the exponent ν smaller than unity gives a more active plastic flow at the GB, whereas a large ν suppresses the plastic flow at the boundary. Kheradmand et al. [2016] suggested that transferability of the GB rapidly decreases when the critical condition $\left|\cos\theta_{\mathrm{AB}}^{(\alpha\beta)}\right|\left|\cos\kappa_{\mathrm{AB}}^{(\alpha\beta)}\right| \le \cos 15^\circ \cdot \cos 15^\circ = 0.933$ holds. If we postulate that a hard-type GB is practically represented with $\phi \approx 0.5$, as is expected from the observation in Figure 2 (left), ν is assumed to be ~ 10.

4. Application to a practical problem: bicrystalline micropillar compression

4.1. ***Problem formulation.*** To illustrate the effect of the higher-order boundary conditions in a practical problem of a small sized body, the bicrystalline micropillar compression problem is considered. The finite element model of an f.c.c. bicrystal micropillar with a square cross section is considered, as shown in Figure 6 (left). The aspect ratio of the gauge length H to the edge length W is selected to be 2.3 [Shade et al. 2012; Kuroda 2013]. A plane GB is assumed at $X_1 = 0$ with an initial unit normal of $\boldsymbol{n}_0^{\mathrm{GB}} = (-1, 0, 0)$ in the undeformed configuration. The portion for $X_1 \ge 0$ is assigned as grain A, and that for $X_1 < 0$ is assigned as grain B. Although the specific material and experimental data are not strictly quoted and no parameter fitting study is intended in the present computations, several practical conditions are taken from the study of Imrich et al. [2014] who employed copper single- and bicrystalline micropillars.

Three models of bicrystalline micropillars with different sets of crystal orientations are considered. The first model includes an arbitrary large-angle grain boundary (LAGB), and the other two models have a coherent twin boundary (CTB). In the LAGB micropillar, the [3 1 0] and [1 $\bar{3}$ 26] directions are chosen to be parallel to the sample axis (the X_3-direction) and X_1-direction, respectively, for grain A. The [4 0 $\bar{1}$]

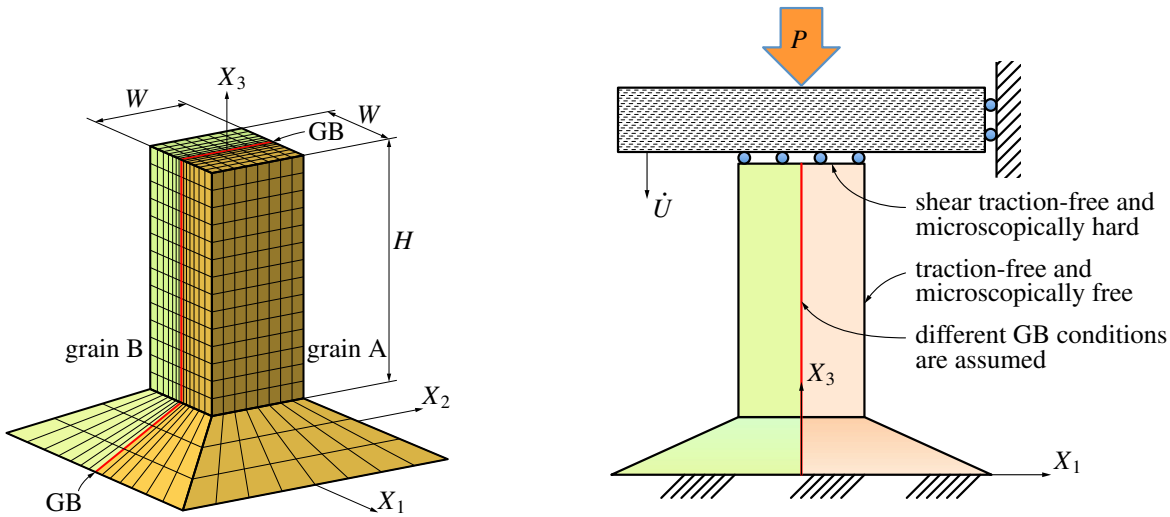

Figure 6. Bicrystalline micropillar compression problem. Finite element model (left); schematic illustration of the boundary conditions (right).

and [3 $\bar{1}$ 12] directions coincide with the X_3- and X_1-directions, respectively, for grain B. The two grains have a difference of 22.8° in orientation around [1 $\bar{3}$ 4]. One of the CTB micropillars, which is designated as CTB-1, has crystal orientations such that the [1 $\bar{1}$ 0] direction is parallel to the X_3-direction and the [1 1 1] direction coincides with the X_1-direction. The crystal orientations of grains A and B are in mirror symmetry about the GB plane, i.e., the orientation of grain A rotated at 180° around the [1 1 1] direction coincides with that of grain B. Each grain has four potentially active slip systems that have the same (highest) Schmid factors = 0.4082 (see [Imrich et al. 2014, Figure 6] for better understanding). Two of these slip systems have the Burgers vectors parallel to the GB plane ($\phi_I^{(i)} = 1$ for the two slip systems). In the other CTB micropillar, which is designated as CTB-2, the crystal orientations considered in CTB-1 are rotated 7.5° about the X_1-axis (counterclockwise rotation in the X_2-X_3 plane). Owing to this tilt, the number of potentially active slip systems is reduced to one in each grain. This unique potentially active slip system has a Schmid factor of 0.4553 and its Burgers vector remains parallel to the GB plane (and also $\phi_I^{(i)} = 1$ for this slip system). All other slip systems have Schmid factors smaller than 0.4. This configuration is rather similar to that of a group of samples employed in [Hirouchi and Shibutani 2014].

The finite strain version of the theory [Kuroda and Tvergaard 2008a] is used. The same theory has already been applied to single-crystal micropillar compression analysis by Kuroda [2013]. The elastic constants are chosen to be $c_{11} = 171$ GPa, $c_{12} = 122$ GPa, and $c_{44} = 69.1$ GPa [Berryman 2005]. The initial slip resistance τ_0 is taken to be 30 MPa for the LAGB micropillar and 50 MPa for the CTB micropillar [Imrich et al. 2014]. The slip hardening modulus h_0 ($= h^{(\alpha\beta)}$) is set to zero for simplicity and also as a reference to the experimental observation of very weak work hardening for single-crystal copper micropillars in [Imrich et al. 2014]. The rate sensitivity parameter m is taken to be 0.05. The length scale l is taken as $l/W = 0.8$.

In the finite element computations, the displacement field is solved using three-dimensional brick-type twenty-node (serendipity) elements with $2 \times 2 \times 2$ Gauss points (i.e., reduced integration) and the GND

density field is solved using three-dimensional brick-type eight-node (bilinear) elements with $2 \times 2 \times 2$ Gauss points (i.e., full integration). The coordinates of the nodes in the eight-node elements are set to be identical to those of the corner nodes in the twenty-node elements.

The axial displacement $\dot{U}$, taken to be positive in the negative X_3-direction, is assigned to the top surface at a nominal strain rate of $\dot{\epsilon}_{\mathrm{N}} = \dot{U}/H = f_{\mathrm{S}}^{(\max)}\dot{\gamma}_0$ with $f_{\mathrm{S}}^{(\max)}$ being the highest absolute values of the nominal Schmid factors among those for all slip systems in the bicrystalline micropillar. A schematic illustration of boundary conditions of the micropillar model is given in Figure 6 (right). A nominal compressive stress is defined as the sum of the nodal forces, P, in the negative X_3-direction, divided by the initial cross-sectional area W^2. Every material point (the nodes in finite element analysis) on the top surface is free to move laterally and will be released from the rigid platen when the normal (contact) stress at that point, which was negative (compressive) at the initial stage of loading, becomes zero. This simply models the case where the friction between the top surface and the loading platen is very low. Regarding the slip rates on the top surface, the microscopically hard condition ($\phi^{(\alpha)} = 0$) is adopted. The contact between the sample top and the loading platen, which are both sufficiently flat, is likely to correspond to this condition. Very few slip lines are often observed on the top surfaces of micropillars after testing (e.g., [Uchic et al. 2004]). This supports the validity of assuming the microscopically hard condition on the top surface. On the traction free surfaces (i.e., on the lateral surface of the gauge region and on the upper surface of the substrate), the microscopically free condition, which corresponds to the null GND condition, is assumed. All the degrees of freedom for displacements on the bottom surface of the substrate are fully constrained, and the microscopically hard condition is assumed on the bottom surface. This setting does not much affect the computational results because essentially the slips are not activated near the bottom surface of the substrate.

Next, we consider the microscopic boundary conditions at the boundary between grains A and B. The following four conditions for the GB are assumed.

Hard GB:	$\phi_I^{(i)} = 0$,
Transparent GB:	$\phi_I^{(i)} = 1$,
Orientation-dependent GB I:	Equations (33) and (34) with $\nu = 1$,
Orientation-dependent GB II:	Equations (33) and (34) with $\nu = 10$.

Although the values of $\bar{C}_{\mathrm{AB}}^{(\alpha\beta)}$ will vary owing to the lattice rotations in each grain under general finite deformations, the updates of $\bar{C}_{\mathrm{AB}}^{(\alpha\beta)}$ are omitted for simplicity and the initial values of $\bar{C}_{\mathrm{AB}}^{(\alpha\beta)}$ are used throughout the computations. This simplification may not significantly affect the results, because the overall nominal compressive strain of the samples will be lower than 10%.

4.2. ***Results.*** The computed curves of nominal compressive stress versus nominal compressive strain for the LAGB, CTB-1, and CTB-2 samples are shown in Figure 7. Computational results using the conventional crystal plasticity model with no account of the size effect [Asaro and Needleman 1985] are also shown in these graphs for comparison. In the case of the hard GB, high strain hardening behavior is observed for all the cases of LAGB, CTB-1, and CTB-2. The significant hardening seen here is solely attributed to the development of the backstresses near the hard GB, around which steep gradients of the slips are generated owing to the constraint on the slips. This typical behavior of the backstresses associated with the accumulation of the GNDs is illustrated in detail in Figures 9 and 10, focusing on

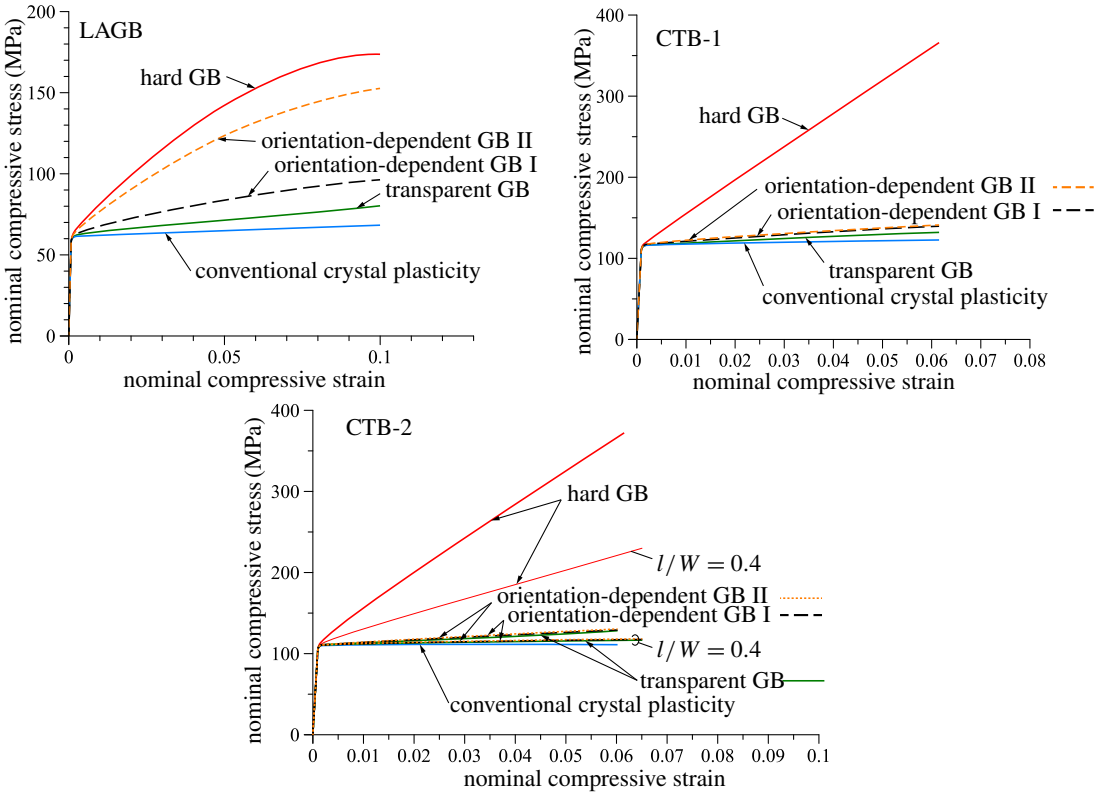

Figure 7. Computed curves of nominal compressive stress versus nominal compressive strain for bicrystalline micropillars with different GB conditions. LAGB samples (left); CTB-1 samples (right); CTB-2 samples (bottom). The length scale is chosen to be $l/W = 0.8$ unless indicated otherwise. In the graphs, "Conventional crystal plasticity" denotes the result obtained using the conventional size-independent crystal plasticity model of Asaro and Needleman [1985]. Orientation-dependent GB II corresponds to $\nu = 10$ and orientation-dependent GB I corresponds to $\nu = 1$.

the results for CTB-2, which has the simplest deformation mechanism and is relevant for understanding the fundamental mechanical behavior.

For LAGB, the computation with the hard GB has predicted high strain hardening behavior, which seems to be consistent with that observed in the experimental stress–strain curve [Imrich et al. 2014]. The orientation-dependent GB II (with $\nu = 10$) also leads to high amounts of strain hardening comparable to that predicted by the hard GB, because the values of $\phi_I^{(i)}$ computed with $\bar{C}_{\mathrm{AB}}^{(\alpha\beta)}$ values of $0 < \bar{C}_{\mathrm{AB}}^{(\alpha\beta)} < 1$ are significantly decreased by the exponent $\nu = 10$. The values of $\phi_I^{(i)}$ for the primary slip systems on the grains A and B sides are respectively 0.360 and 0.525, which give sufficiently hard interface responses as expected from the slip distribution profile shown in Figure 2 (left). The correspondence between the current numerical and the experimental results partly supports the view that LAGB functions as a barrier to dislocations. On the other hand, the orientation-dependent GB I (with $\nu = 1$) and the transparent GB predict a rather low strain hardening behavior.

In the cases of the CTB-1 and CTB-2 samples that have the crystal orientations with the mirror symmetry about the GB plane, the nominal stress-strain curves are nearly linear. The computations with the orientation-dependent GBs (both I and II) exhibit very weak (or almost no) hardening that is consistent with that observed in the experimental stress-strain curves reported in [Imrich et al. 2014] and [Hirouchi and Shibutani 2014]. These curves are close to those for the transparent GB. In the CTB-1 sample, there are four active slip systems in each grain, which have the same highest Schmid factor. Two of these have the Burgers vectors whose directions are parallel to the GB. Even on these slip systems, large amounts of backstresses are produced owing to pileups of screw GNDs when the hard GB is assumed (i.e., a strong slip gradient is produced in the direction perpendicular to the Burgers vector on the slip plane). In the cases of the orientation-dependent GBs (both I and II), these slip systems have $\phi_I^{(i)} = 1$, and thus the GB exhibits no resistance to slips. Such a transparent nature of CTB has already been suggested by Imrich et al. [2014]. The CTB-2 sample explains this condition more clearly due to its simplicity. The CTB-2 sample has only one active slip system whose Burgers vector is parallel to the GB plane in each grain. Hirouchi and Shibutani [2014] conducted compression tests on bicrystalline micropillars having active slip systems nearly parallel to the GB, which are similar to those in the CTB-2 samples. They observed that their stress-strain curves were fundamentally equivalent to those for the single-crystalline samples that showed minimal (almost no) strain hardening. This coincidence supports the view that the CTBs have fundamentally no resistance to slips.

Figure 8 shows the deformations and contours of slips on the primary slip systems whose Burgers vectors are parallel to the GB surface for the CTB-2 samples at a nominal compressive strain of 0.06. The deformation modes predicted with the transparent GB (Figure 8b), the orientation-dependent GB I (Figure 8c) and the orientation-dependent GB II (Figure 8d) are composed of two outer *dead* zones and one distinct central *shear* zone that fully penetrates the body of the pillar. This deformation mode is fairly consistent with the experimental observation by Hirouchi and Shibutani [2014] and it is also similar to that of a single-slip single-crystal micropillar. Comparing the results shown in Figures 8b, 8c, and 8d, the samples with the orientation-dependent GBs (both I and II) exhibited more activated slips on the primary slip systems than the sample with the transparent GB. In these cases, only $\phi_I^{(i)}$ for the slip systems positioned in the cross slip configuration (including the primary slip system) show unity. Smaller values of $\phi_I^{(i)}$ for the other slip systems (including the secondary and tertiary slip systems) indicate the suppression of slip activations at the GB. In the case of the transparent GB, all slip systems have $\phi_I^{(i)} = 1$; thus, the secondary and tertiary slip systems could be activated much more easily than those in the case of the orientation-dependent GBs. Such a distinct appearance of the shear zone may support the properness of the present orientation-dependent GB models. The hard GB does not lead to a visible shear zone and causes less amounts of slip, as shown in Figure 8a. The conventional theory provides no constraint of the slip at every boundary because it has no higher-order microscopic boundary conditions. The conventional theory does not predict the fully penetrating uniform shear zone, but predicts a weakly concentrated and heterogeneous shear area (Figure 8e). Introduction of both the gradient effect and the microscopic boundary conditions is necessary to reproduce the typical deformation mode with the penetrating shear zone, as emphasized by Kuroda [2013].

Figure 9 shows the distributions of the screw GND densities on the primary slip systems in the CTB-2 samples with different GB conditions. In the case of the hard GB (Figure 9 (upper-left)), the screw GNDs significantly accumulate at the GB. In the cases of the transparent GB (Figure 9 (upper-right)),

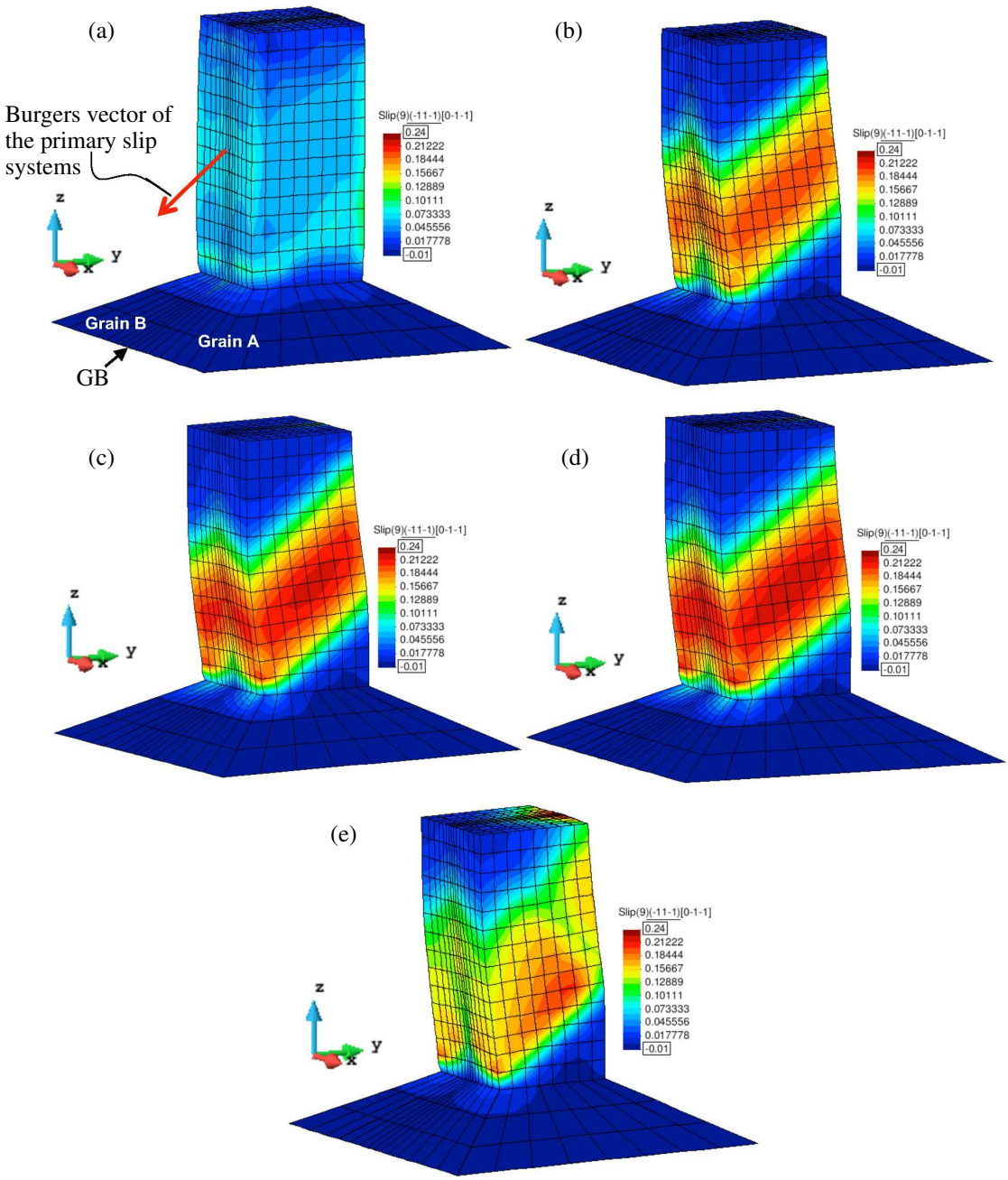

Figure 8. Deformed meshes and contours of slip on the primary slip systems for CBT-2 samples with different GB conditions at a nominal compressive strain of 0.06. The length scale is chosen to be $l/W = 0.8$. The Burgers vectors of the primary slip systems are parallel to the grain boundary. Hard GB (a); transparent GB (b); orientation-dependent GB I ($\nu = 1$) (c); orientation-dependent GB II ($\nu = 10$) (d); conventional size-independent crystal plasticity model (e).

the orientation-dependent GB I (Figure 9 (lower-left)), and the orientation-dependent GB II (Figure 9 (lower-right)), the screw GND densities are much lower than that for the hard GB case. Figure 10 depicts the distributions of the backstresses on the primary slip systems in the CTB-2 samples with different GB conditions. Significant amounts of backstresses were produced at the GB in the case of the hard GB (Figure 10 (upper-left)). The influence of the backstress produced near the GB is observed as apparently strong strain hardening in the stress–strain curves (Figure 7). The backstresses produced in the transparent GB sample (Figure 10 (upper-right)), the orientation-dependent GB I sample (Figure 10 (lower-left)), and the orientation-dependent GB II sample (Figure 10 (lower-right)) are much smaller than that produced in the hard GB samples. Consequently, very small amounts of strain hardening appear in the stress-strain relations and this trend is consistent with experimental observations.

The length scale of $l/W = 0.8$ has been used thus far in the present application shown above. Results for a different value of the length scale, $l/W = 0.4$, are additionally shown in Figure 7 (bottom) for comparison. The nominal stress for the hard GB sample is significantly lowered by the decrease in the length scale. The nominal stresses for the transparent GB sample, the orientation-dependent GB I sample and the orientation-dependent GB II sample become close to that for the conventional plasticity result. But, the overall deformation behaviors of the samples with $l/W = 0.4$ are very similar to those shown in Figures 8–10, although their depictions are omitted.

5. Discussion

5.1. ***On the predictability of the model.*** From the comparison of the present numerical results of the micropillar compression problem with experimental observations in the literature, it can be said that the GB has the transparent nature if the opposite slip systems from the neighboring grains are positioned in the cross slip configuration. The GB models given by (33) with (34), i.e., the orientation-dependent GB I (with $\nu = 1$) and orientation-dependent GB II (with $\nu = 10$) in the application, represent this nature. The experimentally observed mechanical response of the samples with CTB is characterized by these models. The orientation-dependent GB II (with $\nu = 10$) also predicts the experimentally observed material response of the LAGB sample showing the significant amount of strain hardening. This finding partly supports the soundness of the assumption that the amount of slip at the GB nonlinearly depends on the moduli $\bar{C}_{\mathrm{AB}}^{(\alpha\beta)}$. As mentioned in the Introduction, however, opposite observations have been reported [Kunz et al. 2011; Kim et al. 2015], i.e., LAGBs in submicrometer-sized bicrystalline pillars did not act as strong barriers to moving dislocations nor caused additional strain hardening. Such behavior can be apparently described with a low value of ν (e.g., $\nu \approx 1$ or lower), although its physical mechanism is not known at present.

The present model only considers the geometrical configuration of the slip systems and the GB plane. Incorporation of other possible effects, e.g., yielding of the GB at a certain stage of deformation, temperature dependence, and interaction between the GB and the external surface, is left for future studies.

As mentioned in Section 3, in the current model, $\underline{\dot{\gamma}}_{\mathrm{A}}^{(\alpha)}$ at a point on the grain A side of the interface is determined only by the slip rate $\dot{\gamma}_{\mathrm{A}}^{(\alpha)}$ in grain A. A more elaborate formulation of $\underline{\dot{\gamma}}_{\mathrm{A}}^{(\alpha)}$ that also considers the influences of the slip rates $\dot{\gamma}_{\mathrm{B}}^{(\beta)}$ in grain B may be conceived. Such coupling induces a significant complexity in the formulation and also in the computational procedure that demands the use of a kind of *joint element*. This results in a tremendous increase in the size of the system of the equations

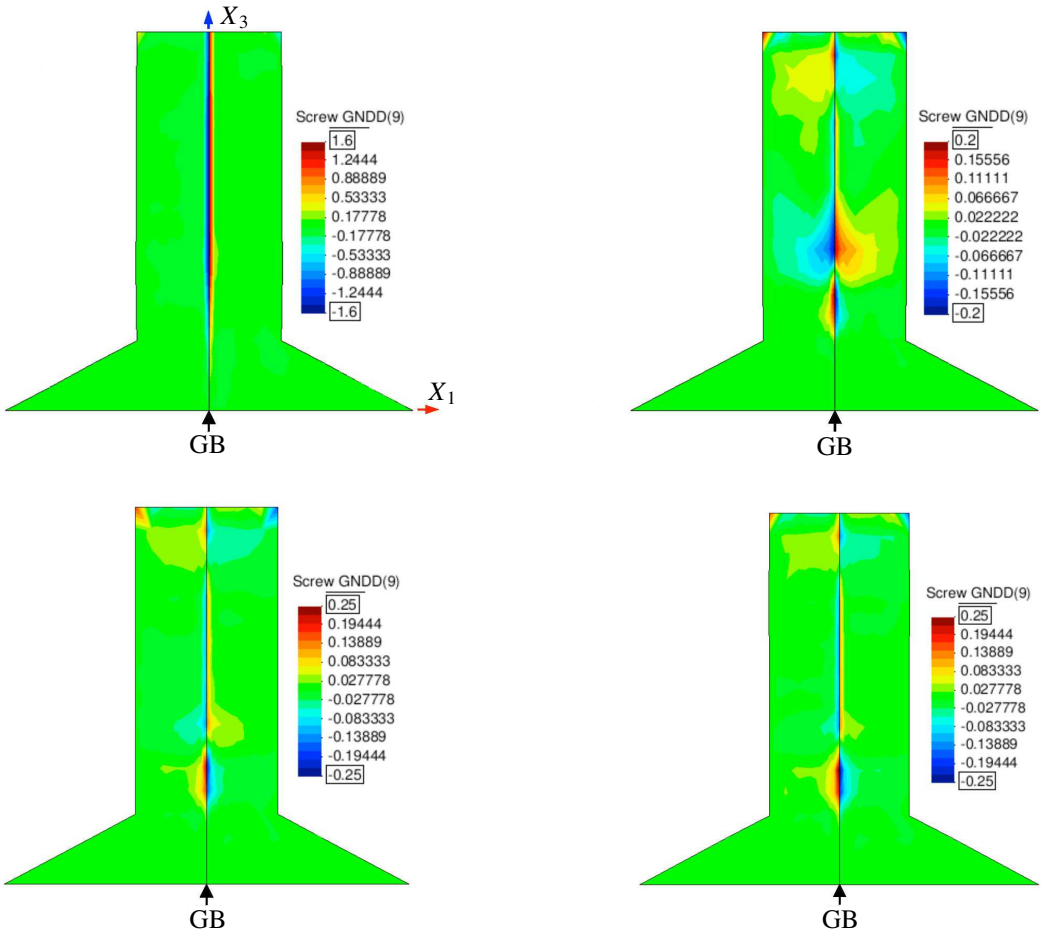

Figure 9. Contours of the screw GND densities (nondimensionalized as $\rho^{(\alpha)}_{\mathrm{G(s)}} bl$) on the primary slip systems in the middle cross section (X_1-X_3 plane views) for CTB-2 samples with different GB conditions at a nominal compressive strain of 0.06. The Burgers vectors of the primary slip systems are parallel to the grain boundary. The length scale is chosen to be $l/W = 0.8$. Hard GB (upper-left); transparent GB (upper-right); orientation-dependent GB I ($\nu = 1$) (lower-left); orientation-dependent GB II ($\nu = 10$) (lower-right).

especially in cases of three-dimensional analysis of a polycrystal. The proposed model with the omission of this coupling is simple. Nevertheless, it has the capability to represent the overall material responses associated with both LAGB and CTB using the same material parameter values.

The present treatment of the microscopic boundary conditions may also efficiently represent peculiar microscopic characteristics of external surfaces. For example, an external surface coated by an incomplete or fragile thin oxide layer that is partially penetrable to dislocations may be modeled by $0 < \phi^{(\alpha)} < 1$ with appropriate constitutive modeling of $\phi^{(\alpha)}$. This is also left for future studies.

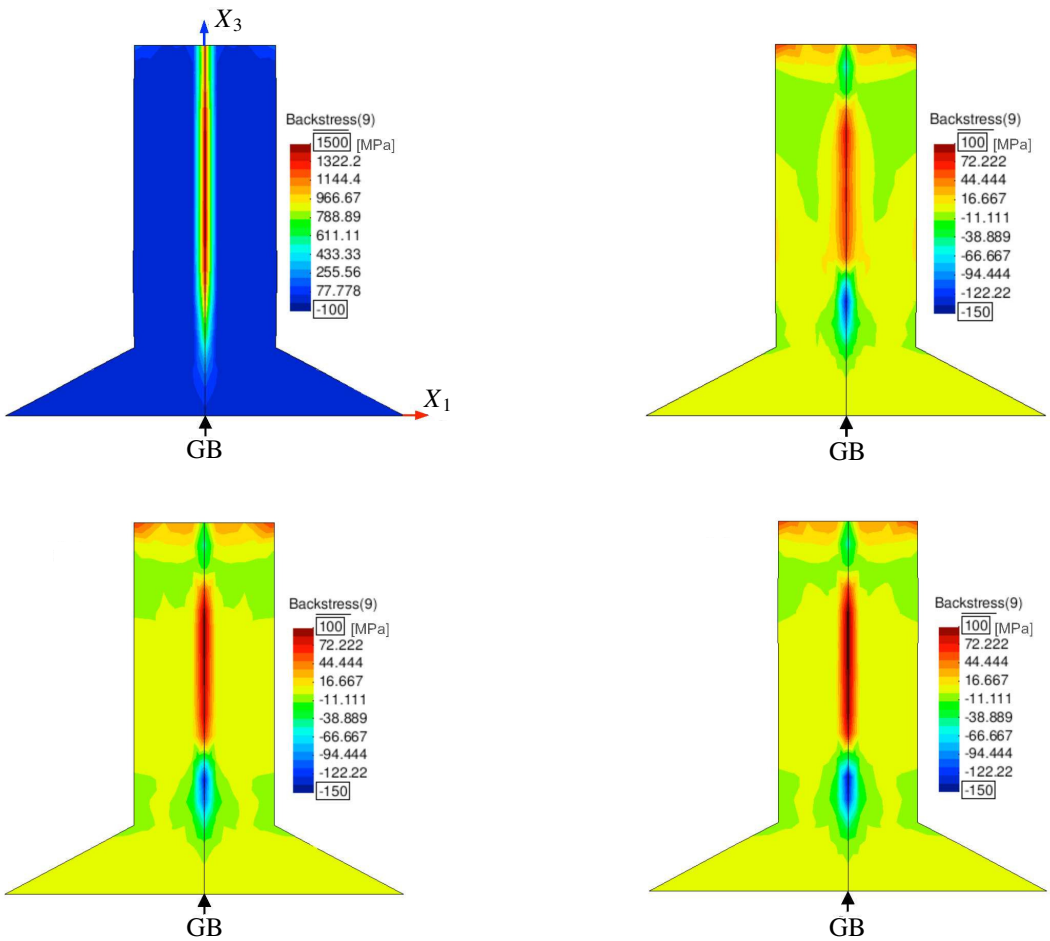

Figure 10. Contours of the backstresses on the primary slip systems in the middle cross section (X_1-X_3 plane views) for CTB-2 samples with different GB conditions at a nominal compressive strain of 0.06. The Burgers vectors of the primary slip systems are parallel to the grain boundary. The length scale is chosen to be $l/W = 0.8$. Hard GB (upper-left); transparent GB (upper-right); orientation-dependent GB I ($\nu = 1$) (lower-left); orientation-dependent GB II ($\nu = 10$) (lower-right).

5.2. ***On the formulation of the model.*** The non-work-conjugate type (or backstress-based) strain gradient plasticity formulation, on which the current theory is based, can be converted to the work-conjugate type representation, as has been discussed by Kuroda and Tvergaard [2006; 2008a; 2008b] and Ertürk et al. [2009]. A virtual work expression that is the basis of the latter type is derived as follows. We use mathematical expressions for the finite strain conditions, referring to [Kuroda and Tvergaard 2008a], but the fundamental points do not differ from those of its small strain version [Kuroda and Tvergaard 2008b]. According to the kinematics of crystal plasticity, the virtual velocity gradient $\tilde{\boldsymbol{L}}$ can be represented by

$$\tilde{\boldsymbol{L}} = \dot{\tilde{\boldsymbol{u}}} \otimes \nabla = \tilde{\boldsymbol{L}}^{\mathrm{e}} + \sum_{\alpha} \dot{\tilde{\gamma}}^{(\alpha)} \bar{\boldsymbol{s}}^{(\alpha)} \otimes \bar{\boldsymbol{m}}^{(\alpha)}, \tag{35}$$

where $\dot{\tilde{\boldsymbol{u}}}$ is a virtual velocity, ∇ is redefined as the spatial gradient operator with respect to the current (deformed) configuration, $\tilde{\boldsymbol{L}}^{\mathrm{e}}$ is a virtual elastic distortion rate, $\dot{\tilde{\gamma}}^{(\alpha)}$ is a virtual slip rate, and $\bar{\boldsymbol{s}}^{(\alpha)}$ and $\bar{\boldsymbol{m}}^{(\alpha)}$ are the slip direction and slip plane normal vectors in the deformed configuration, respectively (a superposed bar denotes that the quantity is evaluated in the deformed configuration). Using the elastic-plastic decomposition of $\tilde{\boldsymbol{L}}$ in (35), the conventional virtual work principle is written as

$$\int_V \left(\boldsymbol{\sigma} : \tilde{\boldsymbol{L}}^{\mathrm{e}} + \sum_\alpha \tau^{(\alpha)} \dot{\tilde{\gamma}}^{(\alpha)} \right) \mathrm{d}V = \int_S \boldsymbol{t} \cdot \dot{\tilde{\boldsymbol{u}}} \, \mathrm{d}S. \tag{36}$$

Here, V and S are respectively the volume and the boundary surface of the body in the deformed configuration.

If the backstress on each slip system can be expressed as the divergence of a vector quantity [7], $\boldsymbol{\xi}^{(\alpha)}$, i.e.,

$$\tau_{\mathrm{b}}^{(\alpha)} = -\nabla \cdot \boldsymbol{\xi}^{(\alpha)}, \tag{37}$$

then we can rewrite the yield condition as

$$\tau^{(\alpha)} + \nabla \cdot \boldsymbol{\xi}^{(\alpha)} = \pi^{(\alpha)} \tag{38}$$

with the definition $\pi^{(\alpha)} = \mathrm{sgn}(\tau^{(\alpha)} + \nabla \cdot \boldsymbol{\xi}^{(\alpha)}) g^{(\alpha)}$, where $g^{(\alpha)}$ is the CRSS of each slip system. Substituting (38) into (36) and applying the divergence theorem and integration by parts, (36) can be further expressed as

$$\int_V \boldsymbol{\sigma} : \tilde{\boldsymbol{L}}^{\mathrm{e}} \, \mathrm{d}V + \sum_\alpha \int_V (\pi^{(\alpha)} \dot{\tilde{\gamma}}^{(\alpha)} + \boldsymbol{\xi}^{(\alpha)} \cdot \nabla \dot{\tilde{\gamma}}^{(\alpha)}) \, \mathrm{d}V = \int_S \boldsymbol{t} \cdot \dot{\tilde{\boldsymbol{u}}} \, \mathrm{d}S + \sum_\alpha \int_S \bar{\boldsymbol{n}} \cdot \boldsymbol{\xi}^{(\alpha)} \dot{\tilde{\gamma}}^{(\alpha)} \, \mathrm{d}S. \tag{39}$$

This equation exactly corresponds to the virtual work principle expression introduced by Gurtin [2002] as the major premise of the theory. In (39), the quantities $\boldsymbol{\xi}^{(\alpha)}$ may be viewed as microscopic stresses that are work-conjugate to the slip rate gradients, and the quantities $\bar{\boldsymbol{n}} \cdot \boldsymbol{\xi}^{(\alpha)}$ appearing on the boundary are considered as *microscopic tractions*.

Next, we consider two pieces of material, grains A and B, as shown in Figure 4 (left), which will form a single body with a GB, as illustrated in Figure 4 (right). The virtual work expression of (39) is applied to each of the grains shown in Figure 4 (left), recognizing the potential GB surfaces $S_{\mathrm{GB(A)}}$ and $S_{\mathrm{GB(B)}}$ with unit normal $\bar{\boldsymbol{n}}_{\mathrm{GB}}$ and $-\bar{\boldsymbol{n}}_{\mathrm{GB}}$, which are respectively expediently distinguished from the outer surfaces S_{A} and S_{B}:

$$\begin{aligned} &\int_{V_{\mathrm{A}}} \boldsymbol{\sigma} : \tilde{\boldsymbol{L}}^{\mathrm{e}} \, \mathrm{d}V + \sum_\alpha \int_{V_{\mathrm{A}}} (\pi^{(\alpha)} \dot{\tilde{\gamma}}^{(\alpha)} + \boldsymbol{\xi}^{(\alpha)} \cdot \nabla \dot{\tilde{\gamma}}^{(\alpha)}) \, \mathrm{d}V \\ &\qquad = \int_{S_{\mathrm{A}}} \boldsymbol{t} \cdot \dot{\tilde{\boldsymbol{u}}} \, \mathrm{d}S + \int_{S_{\mathrm{GB(A)}}} \boldsymbol{t} \cdot \dot{\tilde{\boldsymbol{u}}} \, \mathrm{d}S + \sum_\alpha \left(\int_{S_{\mathrm{A}}} \bar{\boldsymbol{n}} \cdot \boldsymbol{\xi}^{(\alpha)} \dot{\tilde{\gamma}}^{(\alpha)} \, \mathrm{d}S + \int_{S_{\mathrm{GB}(A)}} \bar{\boldsymbol{n}}_{\mathrm{GB}} \cdot \boldsymbol{\xi}^{(\alpha)} \dot{\tilde{\gamma}}^{(\alpha)} \, \mathrm{d}S \right), \end{aligned} \tag{40}$$

[7] If we assume that $\boldsymbol{\xi}^{(\alpha)} = -l^2 b \tau_0 [\bar{\rho}_{\mathrm{G(e)}}^{(\alpha)} \bar{\boldsymbol{s}}^{(\alpha)} + \bar{\rho}_{\mathrm{G(s)}}^{(\alpha)} \bar{\boldsymbol{p}}^{(\alpha)}]$, the backstress relation becomes $\tau_{\mathrm{b}}^{(\alpha)} = l^2 b \tau_0 (\nabla \bar{\rho}_{\mathrm{G(e)}}^{(\alpha)} \cdot \bar{\boldsymbol{s}}^{(\alpha)} + \nabla \bar{\rho}_{\mathrm{G(s)}}^{(\alpha)} \cdot \bar{\boldsymbol{p}}^{(\alpha)} + \bar{\rho}_{\mathrm{G(e)}}^{(\alpha)} \nabla \cdot \bar{\boldsymbol{s}}^{(\alpha)} + \bar{\rho}_{\mathrm{G(s)}}^{(\alpha)} \nabla \cdot \bar{\boldsymbol{p}}^{(\alpha)})$. The last two terms in parentheses on the right-hand side, $\bar{\rho}_{\mathrm{G(e)}}^{(\alpha)} \nabla \cdot \bar{\boldsymbol{s}}^{(\alpha)}$ and $\bar{\rho}_{\mathrm{G(s)}}^{(\alpha)} \nabla \cdot \bar{\boldsymbol{p}}^{(\alpha)}$, were omitted in the numerical computations performed in the present paper. These terms do not have any notable effect when there is only a moderate amount of deformation [Kuroda and Tvergaard 2008a].

$$\int_{V_\mathrm{B}} \boldsymbol{\sigma} : \tilde{\boldsymbol{L}}^\mathrm{e}\,\mathrm{d}V + \sum_\alpha \int_{V_\mathrm{B}} (\pi^{(\alpha)}\dot{\tilde{\gamma}}^{(\alpha)} + \boldsymbol{\xi}^{(\alpha)} \cdot \nabla\dot{\tilde{\gamma}}^{(\alpha)})\,\mathrm{d}V$$
$$= \int_{S_\mathrm{B}} \boldsymbol{t}\cdot\dot{\tilde{\boldsymbol{u}}}\,\mathrm{d}S + \int_{S_{\mathrm{GB(B)}}} \boldsymbol{t}\cdot\dot{\tilde{\boldsymbol{u}}}\,\mathrm{d}S + \sum_\alpha \left(\int_{S_\mathrm{B}} \bar{\boldsymbol{n}}\cdot\boldsymbol{\xi}^{(\alpha)}\dot{\tilde{\gamma}}^{(\alpha)}\,\mathrm{d}S - \int_{S_{\mathrm{GB(B)}}} \bar{\boldsymbol{n}}_\mathrm{GB}\cdot\boldsymbol{\xi}^{(\alpha)}\dot{\tilde{\gamma}}^{(\alpha)}\,\mathrm{d}S \right). \quad (41)$$

Here we assume that no displacement gap (no sliding nor crack opening) at the GB occurs, i.e., $\dot{\tilde{\boldsymbol{u}}}|_\mathrm{A} = \dot{\tilde{\boldsymbol{u}}}|_\mathrm{B}$ and $\boldsymbol{\sigma}|_\mathrm{A}\cdot\bar{\boldsymbol{n}}_\mathrm{GB} - \boldsymbol{\sigma}|_\mathrm{B}\cdot\bar{\boldsymbol{n}}_\mathrm{GB} = \boldsymbol{0}$. Now, we bond grains A and B as depicted in Figure 4 (right), and then consider the addition of (40) and (41),

$$\int_V \boldsymbol{\sigma} : \tilde{\boldsymbol{L}}^\mathrm{e}\,\mathrm{d}V + \sum_\alpha \int_V (\pi^{(\alpha)}\dot{\tilde{\gamma}}^{(\alpha)} + \boldsymbol{\xi}^{(\alpha)}\cdot\nabla\dot{\tilde{\gamma}}^{(\alpha)})\,\mathrm{d}V$$
$$= \int_S \boldsymbol{t}\cdot\dot{\tilde{\boldsymbol{u}}}\,\mathrm{d}S + \sum_\alpha \left(\int_S \bar{\boldsymbol{n}}\cdot\boldsymbol{\xi}^{(\alpha)}\dot{\tilde{\gamma}}^{(\alpha)}\,\mathrm{d}S \right) + \sum_\alpha \left(\int_{S_\mathrm{GB}} \left[(\bar{\boldsymbol{n}}_\mathrm{GB}\cdot\boldsymbol{\xi}^{(\alpha)}\dot{\tilde{\gamma}}^{(\alpha)})|_\mathrm{A} - (\bar{\boldsymbol{n}}_\mathrm{GB}\cdot\boldsymbol{\xi}^{(\alpha)}\dot{\tilde{\gamma}}^{(\alpha)})|_\mathrm{B} \right] \mathrm{d}S \right). \quad (42)$$

According to the expression of (42), we may view the power expenditure at the GB per unit area as

$$\sum_\alpha \{[\![\bar{\boldsymbol{n}}_\mathrm{GB}\cdot\boldsymbol{\xi}^{(\alpha)}\dot{\gamma}^{(\alpha)}]\!]\}, \quad (43)$$

where $[\![\bullet]\!] = (\bullet)|_\mathrm{A} - (\bullet)|_\mathrm{B}$ indicates the jump across S_GB.

Gurtin and Needleman [2005] proposed another expression for the power expenditure at the GB in the small strain context,

$$\sum_\alpha \{[\![\bar{\boldsymbol{n}}_\mathrm{GB}\cdot\boldsymbol{\xi}^{(\alpha)}\dot{\gamma}^{(\alpha)}]\!]\} = \boldsymbol{K} : [\![\dot{\boldsymbol{H}}^\mathrm{p}\cdot(\bar{\boldsymbol{n}}_\mathrm{GB}\times)]\!] \geq 0, \quad (44)$$

where $\boldsymbol{K}$ is an internal force tensor distributed over the GB, which is defined as a power-conjugate to the tensor[8] $[\![\dot{\boldsymbol{H}}^\mathrm{p}\cdot(\bar{\boldsymbol{n}}_\mathrm{GB}\times)]\!]$, where $\dot{\boldsymbol{H}}^\mathrm{p}_I = \sum_\alpha \dot{\gamma}^{(\alpha)}_I \bar{\boldsymbol{s}}^{(\alpha)}_I \otimes \bar{\boldsymbol{m}}^{(\alpha)}_I$ (the subscript I stands for A or B) and the sign of inequality indicates the dissipation condition. In particular, the ideal condition $[\![\dot{\boldsymbol{H}}^\mathrm{p}]\!](\bar{\boldsymbol{n}}_\mathrm{GB}\times) = \boldsymbol{0}$ represents a balanced Burgers vector flow, which means that the flow out of grain A is equal to that into grain B. Gurtin and Needleman [2005] called this the defect-free condition. Okumura et al. [2007] performed finite element analysis of a two-dimensional polycrystal (16 f.c.c. grains) unit cell model with adoption of the defect-free condition at the GBs, and reported that the defect-free condition led to a result rather similar to that predicted with a microfree condition $\bar{\boldsymbol{n}}_\mathrm{GB}\cdot\boldsymbol{\xi}^{(\alpha)}_I = 0$. Later, Gurtin [2008b] proposed another GB model in which constitutive relations are given to the *interfacial microforces*, $\lambda^{(\alpha)}_\mathrm{A} \equiv \bar{\boldsymbol{n}}_\mathrm{GB}\cdot\boldsymbol{\xi}^{(\alpha)}|_\mathrm{A}$ and $\lambda^{(\alpha)}_\mathrm{B} \equiv -\bar{\boldsymbol{n}}_\mathrm{GB}\cdot\boldsymbol{\xi}^{(\alpha)}|_\mathrm{B}$ (that appear in (42) and (43)), via thermodynamic consideration based on the *GB free energy* newly proposed and defined. Computational applications of this GB model have been reported in [Özdemir and Yalçinkaya 2014].

In contrast, in the non-work-conjugate approach on which the current model is based, the weak form of the GND density evolution equation (i.e., (13), (29) and (30)) with the surface integral term gives a deduction of the concomitant boundary conditions. In this context, it is natural to consider directly the boundary conditions for the interfacial slip rate, which can be assumed to represent the resultant effects of absorption, emission, and transmission of the dislocations at the GB.

[8] $(\boldsymbol{a}\times)_{ij} = e_{ikj}a_k$, where $\boldsymbol{a}$ is a vector and e_{ikj} is the permutation symbol.

6. Conclusions

In the present paper, a basic strategy for setting arbitrary interfacial microscopic boundary conditions associated with a backstress-based (non-work-conjugate type) higher-order gradient crystal plasticity theory was proposed. A simple model of the GB behavior was considered, which incorporates a nonlinear dependence of a geometrical correlation between orientations of the slip systems and the GB plane on the amount of slip rate at the GB. The model was examined in analyses of the bicrystalline micropillar compression problem. According to qualitative comparison with the experimental results reported in the literature, the model has the capability to represent the overall material responses associated with both LAGB and CTB using the same material parameter values.

Acknowledgments

This work is partly supported by a JSPS Grant-in-Aid for Scientific Research (B), Grant number KAKENHI 25289001.

References

[Acharya and Bassani 2000] A. Acharya and J. L. Bassani, "Lattice incompatibility and a gradient theory of crystal plasticity", *J. Mech. Phys. Solids* **48**:8 (2000), 1565–1595.

[Aifantis 1984] E. C. Aifantis, "On the microstructural origin of certain inelastic models", *J. Eng. Mater. Tech.* **106**:4 (1984), 326–330.

[Aifantis 1987] E. C. Aifantis, "The physics of plastic deformation", *Int. J. Plasticity* **3**:3 (1987), 211–247.

[Arsenlis and Parks 1999] A. Arsenlis and D. M. Parks, "Crystallographic aspects of geometrically-necessary and statistically-stored dislocation density", *Acta Mater.* **47**:5 (1999), 1597–1611.

[Arsenlis et al. 2004] A. Arsenlis, D. M. Parks, R. Becker, and V. V. Bulatov, "On the evolution of crystallographic dislocation density in non-homogeneously deforming crystals", *J. Mech. Phys. Solids* **52**:6 (2004), 1213–1246.

[Asaro and Needleman 1985] R. J. Asaro and A. Needleman, "Overview no. 42: texture development and strain hardening in rate dependent polycrystals", *Acta Metal.* **33**:6 (1985), 923–953.

[Ashby 1970] M. F. Ashby, "The deformation of plastically non-homogeneous materials", *Philos. Mag.* **21**:170 (1970), 399–424.

[Bacca et al. 2013] M. Bacca, D. Bigoni, F. D. Corso, and D. Veber, "Mindlin second-gradient elastic properties from dilute two-phase Cauchy-elastic composites, part I: Closed form expression for the effective higher-order constitutive tensor", *Int. J. Solids Struct.* **50**:24 (2013), 4010–4019.

[Bardella et al. 2013] L. Bardella, J. Segurado, A. Panteghini, and J. Llorca, "Latent hardening size effect in small-scale plasticity", *Model. Simul. Mater. Sci. Eng.* **21**:5 (2013), 055009.

[Bayerschen et al. 2015] E. Bayerschen, M. Stricker, S. Wulfinghoff, D. Weygand, and T. Böhlke, "Equivalent plastic strain gradient plasticity with grain boundary hardening and comparison to discrete dislocation dynamics", *Proc. R. Soc. A* **471**:2184 (2015), 19.

[Bayley et al. 2006] C. J. Bayley, W. A. M. Brekelmans, and M. G. D. Geers, "A comparison of dislocation induced back stress formulations in strain gradient crystal plasticity: size-dependent mechanics of materials", *Int. J. Solids Struct.* **43**:24 (2006), 7268–7286.

[van Beers et al. 2013] P. R. M. van Beers, G. J. McShane, V. G. Kouznetsova, and M. G. D. Geers, "Grain boundary interface mechanics in strain gradient crystal plasticity", *J. Mech. Phys. Solids* **61**:12 (2013), 2659–2679.

[Berryman 2005] J. G. Berryman, "Bounds and self-consistent estimates for elastic constants of random polycrystals with hexagonal, trigonal, and tetragonal symmetries", *J. Mech. Phys. Solids* **53**:10 (2005), 2141–2173.

[Bittencourt et al. 2003] E. Bittencourt, A. Needleman, M. E. Gurtin, and E. van der Giessen, "A comparison of nonlocal continuum and discrete dislocation plasticity predictions", *J. Mech. Phys. Solids* **51**:2 (2003), 281–310.

[Borg 2007] U. Borg, "A strain gradient crystal plasticity analysis of grain size effects in polycrystals", *Eur. J. Mech. A* **26**:2 (2007), 313–324.

[Clark et al. 1992] W. A. T. Clark, R. H. Wagoner, Z. Y. Shen, T. C. Lee, I. M. Robertson, and H. K. Birnbaum, "On the criteria for slip transmission across interfaces in polycrystals", *Scripta Metall. Mater.* **26**:2 (1992), 203–206.

[Ekh et al. 2011] M. Ekh, S. Bargmann, and M. Grymer, "Influence of grain boundary conditions on modeling of size-dependence in polycrystals", *Acta Mech.* **218**:1 (2011), 103–113.

[El-Naaman et al. 2016] S. A. El-Naaman, K. L. Nielsen, and C. F. Niordson, "On modeling micro-structural evolution using a higher order strain gradient continuum theory", *Int. J. Plasticity* **76** (2016), 285–298.

[Ertürk et al. 2009] İ. Ertürk, J. A. W. van Dommelen, and M. G. D. Geers, "Energetic dislocation interactions and thermodynamical aspects of strain gradient crystal plasticity theories", *J. Mech. Phys. Solids* **57**:11 (2009), 1801–1814.

[Evers et al. 2004] L. P. Evers, W. A. M. Brekelmans, and M. G. D. Geers, "Non-local crystal plasticity model with intrinsic SSD and GND effects", *J. Mech. Phys. Solids* **52**:10 (2004), 2379–2401.

[Fleck et al. 1994] N. A. Fleck, G. M. Muller, M. F. Ashby, and J. W. Hutchinson, "Strain gradient plasticity: theory and experiment", *Acta Metall. Mater.* **42**:2 (1994), 475–487.

[Groma et al. 2003] I. Groma, F. F. Csikor, and M. Zaiser, "Spatial correlations and higher-order gradient terms in a continuum description of dislocation dynamics", *Acta Mater.* **51**:5 (2003), 1271–1281.

[Gurtin 2002] M. E. Gurtin, "A gradient theory of single-crystal viscoplasticity that accounts for geometrically necessary dislocations", *J. Mech. Phys. Solids* **50**:1 (2002), 5–32.

[Gurtin 2008a] M. E. Gurtin, "A finite-deformation, gradient theory of single-crystal plasticity with free energy dependent on densities of geometrically necessary dislocations", *Int. J. Plasticity* **24**:4 (2008), 702–725.

[Gurtin 2008b] M. E. Gurtin, "A theory of grain boundaries that accounts automatically for grain misorientation and grain-boundary orientation", *J. Mech. Phys. Solids* **56**:2 (2008), 640–662.

[Gurtin and Needleman 2005] M. E. Gurtin and A. Needleman, "Boundary conditions in small-deformation, single-crystal plasticity that account for the Burgers vector", *J. Mech. Phys. Solids* **53**:1 (2005), 1–31.

[Gutkin and Aifantis 1999] M. Y. Gutkin and E. C. Aifantis, "Dislocations in the theory of gradient elasticity", *Scripta Mater.* **40**:5 (1999), 559–566.

[Hirouchi and Shibutani 2014] T. Hirouchi and Y. Shibutani, "Mechanical responses of copper bicrystalline micro pillars with $\Sigma 3$ coherent twin boundaries by uniaxial compression tests", *Mater. Trans.* **55**:1 (2014), 52–57.

[Imrich et al. 2014] P. J. Imrich, C. Kirchlechner, C. Motz, and G. Dehm, "Differences in deformation behavior of bicrystalline Cu micropillars containing a twin boundary or a large-angle grain boundary", *Acta Mater.* **73** (2014), 240–250.

[Kheradmand et al. 2016] N. Kheradmand, A. F. Knorr, M. Marx, and Y. Deng, "Microscopic incompatibility controlling plastic deformation of bicrystals", *Acta Mater.* **106** (2016), 219–228.

[Kim et al. 2015] Y. Kim, S. Lee, J. B. Jeon, Y.-J. Kim, B.-J. Lee, S. H. Oh, and S. M. Han, "Effect of a high angle grain boundary on deformation behavior of Al nanopillars", *Scripta Mater.* **107** (2015), 5–9.

[Knorr et al. 2015] A. F. Knorr, M. Marx, and F. Schaefer, "Crack initiation at twin boundaries due to slip system mismatch", *Scripta Mater.* **94** (2015), 48–51.

[Kröner 1963] E. Kröner, "On the physical reality of torque stresses in continuum mechanics", *Int. J. Eng. Sci.* **1**:2 (1963), 261–278.

[Kunz et al. 2011] A. Kunz, S. Pathak, and J. R. Greer, "Size effects in Al nanopillars: single crystalline vs. bicrystalline", *Acta Mater.* **59**:11 (2011), 4416–4424.

[Kuroda 2011] M. Kuroda, "On large-strain finite element solutions of higher-order gradient crystal plasticity", *Int. J. Solids Struct.* **48**:24 (2011), 3382–3394.

[Kuroda 2013] M. Kuroda, "Higher-order gradient effects in micropillar compression", *Acta Mater.* **61**:7 (2013), 2283–2297.

[Kuroda 2015] M. Kuroda, "Strain gradient plasticity: a variety of treatments and related fundamental issues", Chapter 9, pp. 199–218 in *From creep damage mechanics to homogenization methods: a liber amicorum to celebrate the birthday of Nobutada Ohno*, edited by H. Altenbach et al., Advanced Structural Materials **64**, Springer, Cham, 2015.

[Kuroda and Tvergaard 2006] M. Kuroda and V. Tvergaard, "Studies of scale dependent crystal viscoplasticity models", *J. Mech. Phys. Solids* **54**:9 (2006), 1789–1810.

[Kuroda and Tvergaard 2008a] M. Kuroda and V. Tvergaard, "A finite deformation theory of higher-order gradient crystal plasticity", *J. Mech. Phys. Solids* **56**:8 (2008), 2573–2584.

[Kuroda and Tvergaard 2008b] M. Kuroda and V. Tvergaard, "On the formulations of higher-order strain gradient crystal plasticity models", *J. Mech. Phys. Solids* **56**:4 (2008), 1591–1608.

[Levkovitch and Svendsen 2006] V. Levkovitch and B. Svendsen, "On the large-deformation- and continuum-based formulation of models for extended crystal plasticity", *Int. J. Solids Struct.* **43**:24 (2006), 7246–7267.

[Mindlin 1964] R. D. Mindlin, "Micro-structure in linear elasticity", *Arch. Rational Mech. Anal.* **16** (1964), 51–78.

[Ng and Ngan 2009] K. S. Ng and A. H. W. Ngan, "Deformation of micron-sized aluminium bi-crystal pillars", *Philos. Mag.* **89**:33 (2009), 3013–3026.

[Ohashi 2005] T. Ohashi, "Crystal plasticity analysis of dislocation emission from micro voids", *Int. J. Plasticity* **21**:11 (2005), 2071–2088.

[Okumura et al. 2007] D. Okumura, Y. Higashi, K. Sumida, and N. Ohno, "A homogenization theory of strain gradient single crystal plasticity and its finite element discretization", *Int. J. Plasticity* **23**:7 (2007), 1148–1166.

[Özdemir and Yalçinkaya 2014] İ. Özdemir and T. Yalçinkaya, "Modeling of dislocation-grain boundary interactions in a strain gradient crystal plasticity framework", *Comput. Mech.* **54**:2 (2014), 255–268.

[Peirce et al. 1983] D. Peirce, R. J. Asaro, and A. Needleman, "Material rate dependence and localized deformation in crystalline solids", *Acta Metallurgica* **31**:12 (1983), 1951–1976.

[Shade et al. 2012] P. A. Shade, M. D. Uchic, D. M. Dimiduk, G. B. Viswanathan, R. Wheeler, and H. L. Fraser, "Size-affected single-slip behavior of René N5 microcrystals", *Mater. Sci. Eng. A* **535** (2012), 53–61.

[Uchic et al. 2004] M. D. Uchic, D. M. Dimiduk, J. N. Florando, and W. D. Nix, "Sample dimensions influence strength and crystal plasticity", *Science* **305**:5686 (2004), 986–989.

[Wulfinghoff et al. 2013] S. Wulfinghoff, E. Bayerschen, and T. Böhlke, "A gradient plasticity grain boundary yield theory", *Int. J. Plasticity* **51** (2013), 33–46.

[Yamada et al. 1968] Y. Yamada, N. Yoshimura, and T. Sakurai, "Plastic stress-strain matrix and its application for the solution of elastic-plastic problems by the finite element method", *Int. J. Mech. Sci.* **10**:5 (1968), 343–354.

[Yefimov et al. 2004a] S. Yefimov, E. van der Giessen, and I. Groma, "Bending of a single crystal: discrete dislocation and nonlocal crystal plasticity simulations", *Model. Simul. Mater. Sci. Eng.* **12**:6 (2004), 1069.

[Yefimov et al. 2004b] S. Yefimov, I. Groma, and E. van der Giessen, "A comparison of a statistical-mechanics based plasticity model with discrete dislocation plasticity calculations", *J. Mech. Phys. Solids* **52**:2 (2004), 279–300.

Received 20 May 2016. Revised 13 Aug 2016. Accepted 13 Sep 2016.

MITSUTOSHI KURODA: kuroda@yz.yamagata-u.ac.jp
Graduate School of Science and Engineering, Mechanical Systems Engineering, Yamagata University, Jonan 4-3-16, Yonezawa, Yamagata 992-8510, Japan

JOURNAL OF MECHANICS OF MATERIALS AND STRUCTURES

msp.org/jomms

Founded by Charles R. Steele and Marie-Louise Steele

Cover photo: Mando Gomez, www.mandolux.com

See msp.org/jomms for submission guidelines.

JoMMS (ISSN 1559-3959) at Mathematical Sciences Publishers, 798 Evans Hall #6840, c/o University of California, Berkeley, CA 94720-3840, is published in 10 issues a year. The subscription price for 2017 is US $615/year for the electronic version, and $775/year (+$60, if shipping outside the US) for print and electronic. Subscriptions, requests for back issues, and changes of address should be sent to MSP.

JoMMS peer-review and production is managed by EditFLOW® from Mathematical Sciences Publishers.

PUBLISHED BY

mathematical sciences publishers

nonprofit scientific publishing

http://msp.org/

Journal of Mechanics of Materials and Structures

Volume 12, No. 2 March 2017